AN ABSTRACT OF THE THESIS OF

Igor Vytyaz for the degree of Master of Science in

Electrical and Computer Engineering presented on December 16, 2005.

Title: Comparison of Time-Domain and Frequency-Domain

Phase Noise Analyses

Abstract approved: _____

Kartikeya Mayaram Un-Ku Moon

This thesis presents a comparison of time-domain and frequency-domain algorithms for phase noise calculation in oscillators. Floquet theory provides the mathematical foundation for these calculations and the numerical methods employ perturbation projection vectors (PPVs). The PPVs are an estimate of an oscillator's sensitivity to noise.

The in-house circuit simulator SPICE3 has been extended to phase noise analysis based on both the time-domain and frequency-domain periodic steady-state analyses. These analysis methods have been evaluated on a wide suite of test oscillators. A detailed comparison of these methods is carried out in terms of accuracy and computation costs. The SPICE3 version with PPV calculation and phase noise analysis is a powerful tool for design of noise tolerant oscillators.

# Comparison of Time-Domain and Frequency-Domain Phase Noise Analyses

by
Igor Vytyaz

A THESIS

submitted to

Oregon State University

in partial fulfillment of
the requirements for the
degree of

Master of Science

Presented December 16, 2005
Commencement June 2006

Master of Science thesis of Igor Vytyaz presented on December 16, 2005

APPROVED:

---

Major Professor, representing Electrical and Computer Engineering

---

Co-Major Professor, representing Electrical and Computer Engineering

---

Director of the School of Electrical Engineering and Computer Science

---

Dean of the Graduate School

I understand that my thesis will become part of the permanent collection of Oregon State University libraries. My signature below authorizes release of my thesis to any reader upon request.

---

Igor Vytyaz, Author

# ACKNOWLEDGEMENTS

During my studies here at Oregon State University, my professors, friends, and family have given me priceless assistance. I would like to take this opportunity to express my sincere appreciation to all these people.

In the first place, I would like to express my utmost gratitude to my advisor Kartikeya Mayaram for giving me an opportunity, both financial and intellectual, to start and accomplish this work. Without his support and insights, none of this work would have been possible. I also thank Prof. Un-Ku Moon for serving as a co-advisor and for his circuits insight.

I would like to express my warm thanks to Taras Dudar and Vova Kratyuk for referring me to my Professor and helping me with initiation of my study here.

My parents, Oleg and Larisa, and my brother Oleksii kept bringing me their love and support, when I was far away from home. They have helped me to finish what I started. Special thanks to my patient and loving wife Ira, who has been a great source of strength through out this work.

Many thanks to my many friends, but especially to Oleksii Fedorenko and Volodymyr Kratyuk for their friendship and support during my years of study. I am thankful to my friends from Ansoft, J.P. Barnard and Chin Siong, to my friends from KPI and from the International House, to my lab mates in Dearborn 212 and Kelley 4130 for their friendship, and useful and inspiring conversations about my work and unrelated topics.

I would like to thank my internship mentors and supervisors, Ramana Aisola from Maxim, Sani Nassif and Frank Liu from IBM, Deepak Ramaswamy, Danil Kirsanov and Saeed Asgari from Ansoft for sharing their experience and their encouragment.

Finally, I would like to acknowledge financial support from NSF and SRC.

I may have forgotten someone. I apologize for my oversight in advance.

TABLE OF CONTENTS

Page

LIST OF FIGURES

LIST OF FIGURES (Continued)

Figure Page

LIST OF TABLES

Table Page

# Comparison of Time-Domain and Frequency-Domain Phase Noise Analyses

## 1. INTRODUCTION

### 1.1. Background and Motivation

During the past decade the popularity of wireless products has grown rapidly. Due to an increase in the number of customers, new communication standards use limited allocated spectrum range with the highest possible efficiency. This is done by accommodating a large number of channels with narrow band widths. The density of communication channels depends on the spectral purity of the local oscillators (LO) in transmitters and receivers [1]. Figure 1.1 shows how the LOs are used for up- and down-conversion of the signal. In the transmitter,

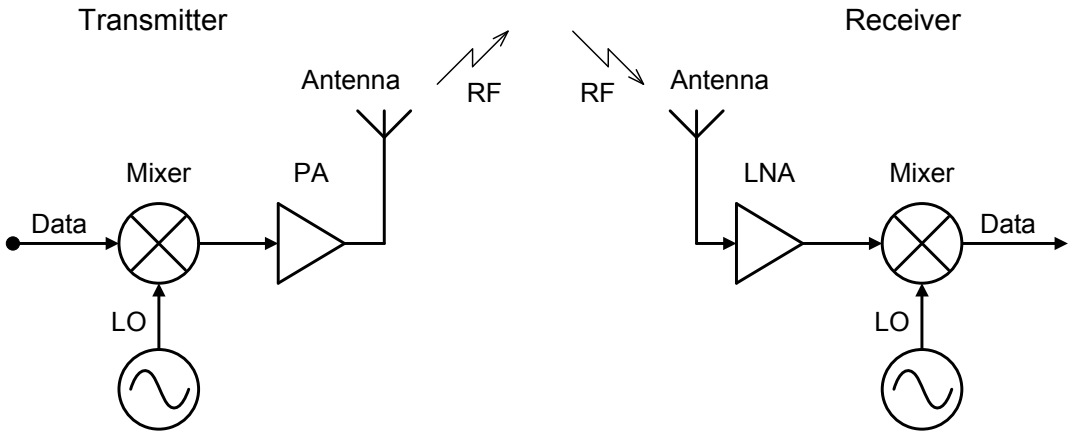


Figure 1.1. Transmitter and receiver block diagrams.

the data signal is upconverted by mixing with an LO signal, it is then amplified by a power amplifier (PA) and transmitted. A transmitter's upconversion oscillator with a noisy spectrum results in energy leakage to adjacent bands [2] and causes interchannel interference. This interference is depicted in Figure 1.2.

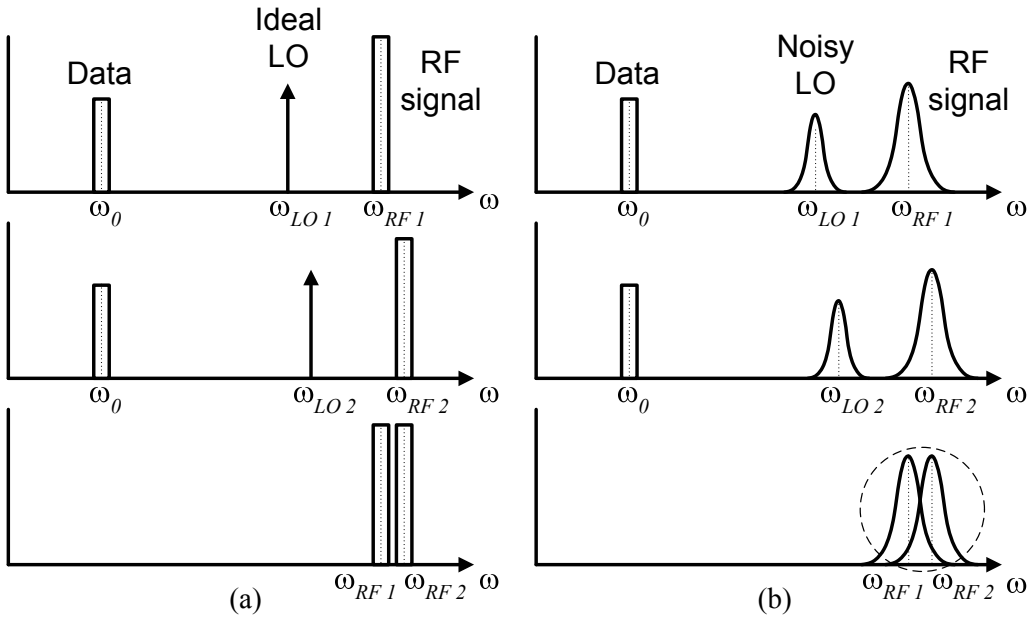


Figure 1.2. Channel interference due to a transmitter's LO.
(a) Upconversion with ideal LOs. (b) Upconversion with noisy LOs.

Figure 1.2(a) shows that data signals, upconverted into two adjacent RF channels by mixing with ideal LO signals, stay within their channel bandwidths. RF signals in the adjacent channels interfere with each other if noisy oscillators are used for upconversion (Figure 1.2(b)).

In the receiver front-end, the received radio-frequency signal is passed to a low noise amplifier (LNA) and downconverted by mixing with the LO signal from the oscillator. In the presence of a strong unwanted RF signal in a neighboring band, a noisy oscillator in the receiver causes channel interference. In Figure 1.3(a) data signals obtained by downconversion of RF signals using an ideal LO signal do not interfere with each other. However, data obtained using a noisy LO is distorted by a strong downconverted RF signal from a neighboring band (Figure 1.3(b)).

In both of these cases, the signal-to-noise ratio (SNR) of the received signal is degraded by a noisy oscillator.

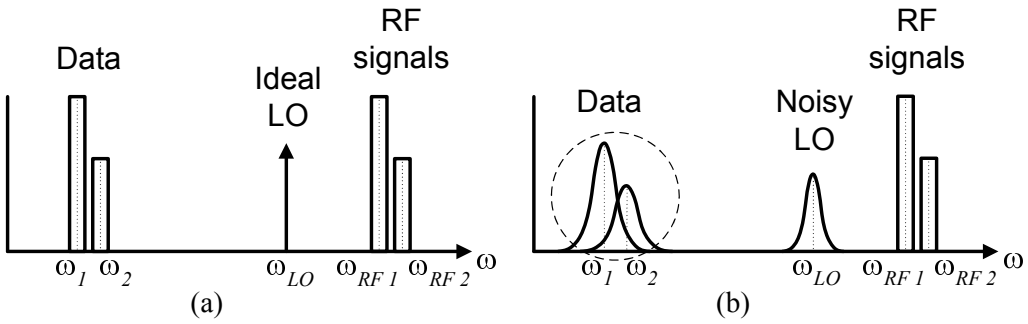


Figure 1.3. Channel interference due to a receiver's LO.
(a) Downconversion with an ideal LO. (b) Downconversion with a noisy LO.

Oscillators are also used in digital systems. One of these applications is clock skew reduction. A noisy oscillator causes synchronization problems, which results in a degradation of the bit-error rate (BER) and limits the frequency of operation, and therefore, the performance of a digital system [1].

From the above description, it is clear that oscillators with low noise need to be designed. The phase noise of an oscillator (see Section 2.1) is a property that characterizes the spectral purity of the oscillator's output signal and its timing characteristics. It is important to predict the phase noise of an oscillator during the design stage through simulation.

Circuit simulation is an important part of an integrated circuit (IC) design flow [3]. It decreases the number of costly and time-consuming chip fabrication cycles required for an operational IC. Once a mathematical model of a circuit is created, the circuit design can be simulated and refined iteratively. When the simulated performance of a circuit design satisfies the given specifications the design is sent for fabrication. For this reason, circuit simulators must support phase noise analysis.

An oscillator's phase noise analysis provides an understanding of the oscillator's spectrum characteristics and its sensitivity to external noise, such as substrate noise or power supply noise. Phase noise analysis can be performed using either the time-domain or the frequency-domain response of an oscillator. Various phase noise analysis techniques have much in common but there are important differences. These are of interest to both circuit-simulator developers and designers who use the circuit simulator as a tool.

The contribution of this thesis is in the implementation of phase noise calculation techniques that work in conjunction with either the time-domain or the frequency-domain periodic steady-state (PSS) analyses. These phase noise techniques are now available in our version of the public-domain circuit simulator SPICE3. A detailed evaluation of the performance of the implemented techniques in terms of accuracy, speed, and scalability is also provided. This then leads to a comparison between the accuracy and speed of the time-domain and frequency-domain analyses.

### 1.2. Thesis Outline

The thesis is organized as follows. Chapter 1 introduces the phase noise problem and provides a motivation for this work. Chapter 2 presents the mathematical theory and numerical methods for phase noise calculation. In Chapter 3 the frequency-domain technique is applied to a set of test oscillator circuits. Then the simulation results are compared with phase noise simulation results from the time-domain based method. A comparison of the simulation performance of the different techniques is presented. Finally, in Chapter 4, conclusions and possible directions for future work are summarized.

# 2. PHASE NOISE THEORY AND NUMERICAL METHODS

This chapter describes the various phase noise calculation techniques and is organized as follows. First, the definitions of phase noise and timing jitter are given. Then Floquet theory and a perturbation analysis for ordinary differential equations (ODE) are presented. The perturbation analysis is based on perturbation projection vectors (PPV). Time- and frequency-domain algorithms for calculation of the PPVs are also described. The singular value decomposition (SVD) solver for the frequency-domain calculation of the PPVs is chosen based on theoretical and practical comparisons of two different SVD solvers.

## 2.1. Phase Noise and Timing Jitter

Let the output of an unperturbed free-running oscillator be denoted as $x_s(t)$. This is a periodic waveform with a period $T$. In the frequency domain $x_s(t)$ is represented by its power spectral density (PSD) $S_x(f)$. For a purely periodic signal the PSD is a sequence of impulses at multiples of the oscillation frequency $f_{osc} = 1/T$ as shown in Figure 2.1. In practice, noise from semiconductor devices,

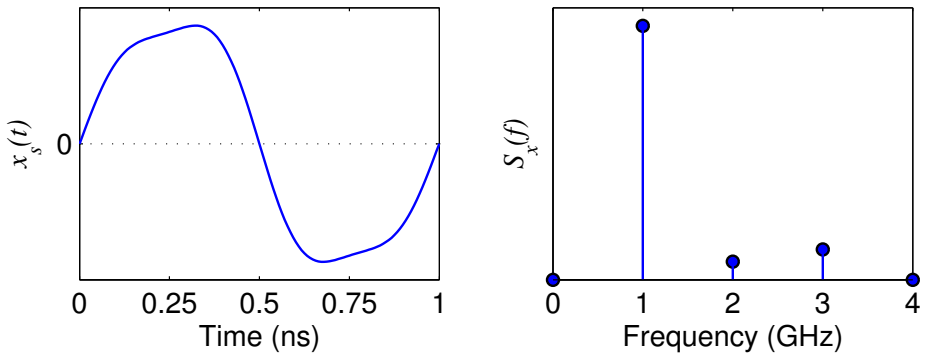


Figure 2.1. Output waveform of an unperturbed oscillator and its PSD.

substrate noise, etc., cause frequency instabilities. A perturbed oscillator's output can be represented as $x_s(t+\alpha(t))+a(t)$, where $\alpha(t)$ describes the phase deviations

and $a(t)$ represents deviations of the amplitude [4]. Figure 2.2 shows the output of an oscillator with phase deviations.

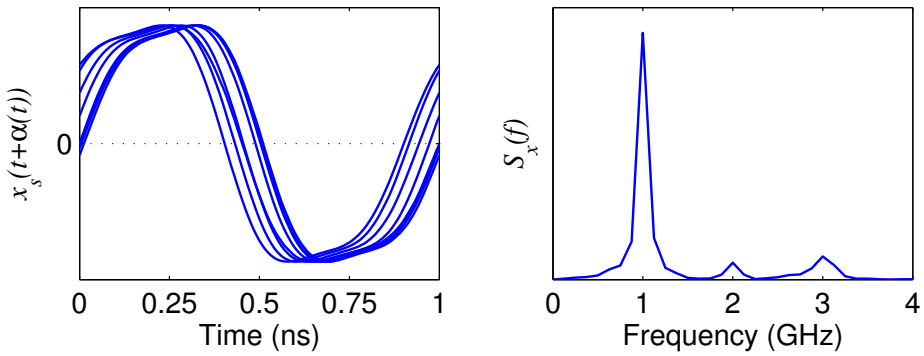


Figure 2.2. Output waveform of a perturbed oscillator and its PSD.

Due to phase deviations, the period of an oscillator at each cycle is different, and there is an uncertainty in the zero-crossing point of $x_s(t + \alpha(t))$ as shown in Figure 2.3. The *cycle-to-cycle jitter* is a statistical measure of the uncertainty in

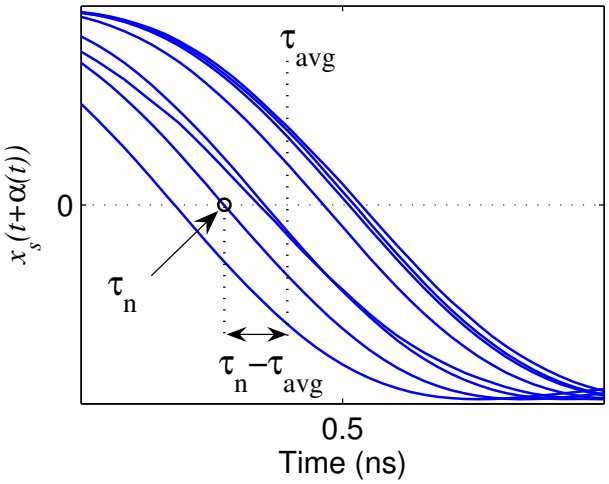


Figure 2.3. Zero crossings of a perturbed oscillator's output.

the zero crossings [5], [6]. It measures the variance of each period with respect to the average period:

$$\sigma_c^2 = \lim_{N\to\infty}\left(\frac{1}{N}\sum_{n=1}^{N}(\tau_n - \tau_{avg})^2\right) \tag{2.1}$$

One can also express the cycle-to cycle jitter in terms of a noise constant $c$, which is a scalar constant that characterizes both the timing jitter and the spectral spreading in a noisy oscillator [4]:

$$\sigma_c^2 = \frac{c}{f_{osc}} \tag{2.2}$$

The spectrum of a perturbed oscillator in Figure 2.2 has sidebands around the frequency of oscillation $f_{osc}$ and its harmonics ($2f_{osc}$, $3f_{osc}$, ...). These are generally referred as the *phase noise* sidebands [1]. In the frequency domain an oscillator's instabilities are characterized by a single sideband (SSB) noise spectral density $\mathcal{L}(f_m)$. The units of $\mathcal{L}(f_m)$ are (dBc/Hz), i.e., decibels below the carrier per Hertz. $\mathcal{L}(f_m)$ is defined as the power of $S_x(f)$ in a 1Hz band around the $f_{osc} + f_m$ frequency, normalized to the total power of $S_x(f)$ around the frequency of oscillation [1]:

$$\mathcal{L}(f_m) = 10log_{10}\frac{P_{1Hz}(f_m)}{P_{carrier}} \tag{2.3}$$

where $f_m$ is the offset from the carrier frequency, as shown in Figure 2.4.

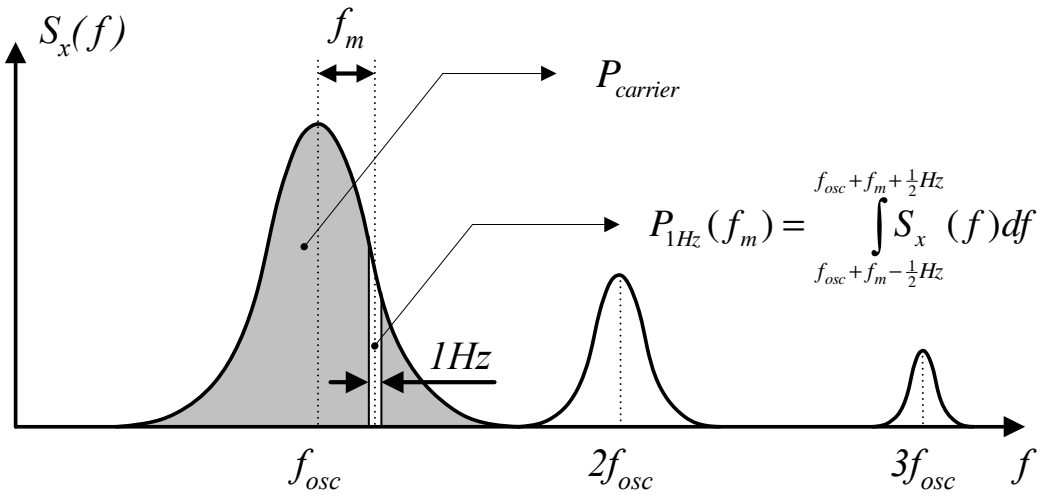


Figure 2.4. Oscillator spectrum and characterization of SSB phase noise.

The definition of $\mathcal{L}(f_m)$ in Equation (2.3) takes into account the effects of the phase deviation $\alpha(t)$ and the amplitude deviation $a(t)$.

The single sideband noise spectral density $\mathcal{L}(f_m)$ can be approximated as a function of the noise constant $c$ [4]:

$$\mathcal{L}(f_m) = 10log_{10}\frac{f_{osc}^2 c}{\pi^2 f_{osc}^4 c^2 + f_m^2} \tag{2.4}$$

As we will see later in Section 2.5, the noise constant $c$ itself is a function of the offset frequency $f_m$.

The noise from various noise sources is projected into the noise constant $c$ by the perturbation projection vectors (PPVs). Floquet theory and perturbation analysis provide the mathematical background for calculation of the PPVs.

## 2.2. Floquet Theory

Consider a linear periodic time-varying (LPTV) system of homogeneous ordinary differential equations (ODE):

$$\dot{x} = A(t)x \tag{2.5}$$

where $A(t)$ is a $T$-periodic $n \times n$ matrix. There can be $n$ linearly independent solutions of Equation (2.5) [7]. These solutions form a linear $n$-dimensional space of solutions $X(t) = [x_1(t), \ldots, x_n(t)]$, which is also called the fundamental matrix. Any solution of Equation (2.5), $x(t)$, can be represented as a linear combination of the columns of the fundamental matrix $X(t)$, i.e.,

$$x(t) = \sum_{i=1}^{n} k_i x_i(t) = X(t)k \tag{2.6}$$

where $k$ is a vector of coefficients $k_i$ that map the columns of $X(t)$ into $x(t)$. If the fundamental matrix is an identity matrix at time $t_0$, $X(t_0) = I_n$, then it is called the state-transition matrix $\Phi(t, t_0)$. The solution $x(t)$ can be determined as

$$x(t) = \Phi(t, t_0)x(t_0) \tag{2.7}$$

The state-transition matrix at time $t_0 + T$ is referred to as a monodromy matrix, $\Phi(t_0 + T, t_0)$ [8]. The monodromy matrix maps the system state at some time $t$ into the future state at time $t + T$.

$$x(t + T) = \Phi(t + T, t)x(t) \tag{2.8}$$

The matrices $\Phi(t+T, t)$ describe the properties of (2.5) and indicate whether the system exhibits growing, decaying, or oscillatory behavior. For any time $t$, the monodromy matrices $\Phi(t+T, t)$ are *similar*, i.e., they are related to each other by a similarity transformation $M^{-1}\Phi M$. This implies that the spectrum of $\Phi(t+T, t)$ is independent of $t$ and is defined by the system (2.5) [7]. This spectrum describes the behavior of the system. The eigenvalues of $\Phi(T, 0)$ are called the characteristic (Floquet) multipliers of the system. If $\lambda_i$ is a characteristic multiplier of the system, then a non-trivial solution $x_k(t)$ exists, such that

$$u_i(t + T) = \lambda_i u_i(t) \tag{2.9}$$

and $u_i(t)$ is an eigenvector of $\Phi(t + T, t)$ that corresponds to the eigenvalue $\lambda_i$.

The state-transition matrix $\Phi(t, s)$ can be represented [9] as

$$\Phi(t, s) = U(t)D(t - s)V(s) = \sum_{i=1}^{n} \lambda_i(t - s)u_i(t)v_i^T(s) \tag{2.10}$$

where the columns of $U(t)$, $u_i(t)$ are the eigenvectors of $\Phi(t + T, t)$, the rows of $V(t) = U^{-1}(t)$, $v_i^T(t)$ are the transposed eigenvectors of $\Phi^T(t + T, t)$, $D$ is a diagonal matrix spanned by $\lambda_i(t) = e^{\mu_i t}$, $\lambda_i(T) = \lambda_i$. The numbers $\mu_i$ are called the characteristic (Floquet) exponents of the system (2.5). Let us substitute (2.10) into (2.7) and represent the initial condition $x(0)$ as a summation of the rows of $U(0)$ scaled by the coefficients $k_j$:

$$x(t) = \Phi(t, 0)x(0) = \sum_{i=1}^{n} \lambda_i(t)u_i(t)v_i^T(0) \cdot \sum_{j=1}^{n} k_j u_j(0) \tag{2.11}$$

Using the fact that $u_i(t)$ and $v_i(t)$ are biorthogonal, i.e., $v_i^T(t)u_j(t) = \delta_{ij}$ (Kronecker delta), particularly when $t = 0$, $x(t)$ can be written as a summation of the eigen modes of the system:

$$\begin{aligned} x(t) &= \lambda_1(t)u_1(t) \cdot k_1 \\ &+ \lambda_2(t)u_2(t) \cdot k_2 \\ &+ \dots \\ &+ \lambda_n(t)u_n(t) \cdot k_n \end{aligned} \tag{2.12}$$

The system (2.5) has an asymptotic orbitally stable solution $x(t)$ if [7]

$$Re(\mu_n) \leq \dots \leq Re(\mu_2) < \mu_1 = 0 \tag{2.13}$$

or equivalently

$$|\lambda_n| \leq \dots \leq |\lambda_2| < \lambda_1 = 1 \tag{2.14}$$

as $\mu_i$ and $\lambda_i$ are related by

$$\lambda_i = e^{\mu_i T} \tag{2.15}$$

In this case, the first component in (2.12), $\lambda_1(t)u_1(t)k_1$, is a stationary component of the solution $x(t)$, also called the oscillatory eigen mode, while the remaining components are the decaying eigen modes that die out after a sufficiently long time. The perturbation analysis is based on the fact that the stationary component of the solution $x(t)$ is aligned along $u_1(t)$.

### 2.3. Perturbation Analysis for ODEs

Let $b(t)$ be a $T$-periodic $n$-vector of perturbations to the system (2.5). Then a perturbed system of ODEs is represented by

$$\dot{x} = A(t)x + b(t) \tag{2.16}$$

The solution for Equation (2.16) can be written in terms of the solution of the unperturbed system (2.5) as $x(t+\alpha(t))+a(t)$, where $a(t)$ is the amplitude deviation and $\alpha(t)$ is the phase deviation. Figure 2.5 shows that a single perturbation $b_a$ at some time $t$ may cause only an amplitude deviation. In Figure 2.6 another

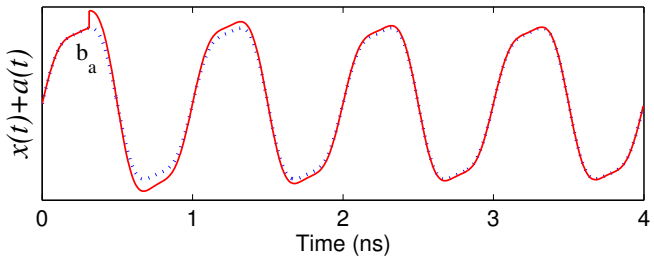


Figure 2.5. Perturbation $b_a$ causes only amplitude deviation.

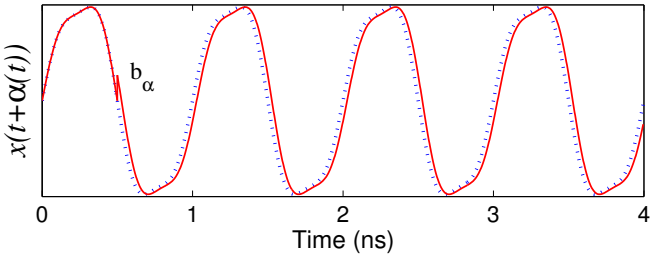


Figure 2.6. Perturbation $b_\alpha$ causes only phase deviation.

perturbation $b_\alpha$ is shown, that results only in a phase deviation. Here, $b_a$ and $b_\alpha$ were applied to a system satisfying conditions (2.14), i.e., with an asymptotic orbitally stable solution $x(t)$. Generally, a perturbation vector $b(t)$ can cause both amplitude and phase deviations, and it is useful to represent it as a superposition of two perturbation vectors:

$$b(t) = b_\alpha(t) + b_a(t) \tag{2.17}$$

where $b_\alpha(t)$ is a perturbation that causes only a phase deviation $\alpha(t)$, and $b_a(t)$ changes only the amplitude by $a(t)$ [10].

As seen from Figures 2.5 and 2.6, the amplitude deviation dies out after some time and the phase deviation remains forever. Our goal is to extract

$b_\alpha(t)$, the component of the perturbation vector $b(t)$ that results only in a persistent phase deviation. The component $b_\alpha(t)$ is aligned with the oscillatory eigen mode $u_1(t)$ of the system, while the component $b_a(t)$ lies in the space spanned by $u_2(t), \ldots, u_n(t)$, i.e., the decaying eigen-modes.

$$b(t) = b_\alpha(t) + b_a(t) = c_1(t)u_1(t) + \sum_{i=2}^{n} c_i(t)u_i(t) \tag{2.18}$$

The time-dependent scalar $c_1(t)$ is a measure of how much of $b(t)$ is projected onto the phase deviation.

## 2.4. Calculation of PPVs

If $u_1(t), \ldots, u_n(t)$ form an orthogonal basis, i.e., the system (2.5) is self-adjoint, then $c_1(t)$ can be calculated as an orthogonal projection of $b(t)$ onto $u_1(t)$ [10]. Unfortunately, linearization of the oscillator model at the periodic steady state generally does not give rise to a self-adjoint system. Therefore, all the eigen modes $u_i(t),\ i = 1, \ldots, n$ have to be calculated to extract $c_1(t)$ from

$$U(t)c(t) = b(t) \tag{2.19}$$

This requires computation of a sequence of monodromy matrices $\Phi(t+T, t)$ for each time $t \in [0, T)$ and a complete eigenvalue decomposition of these matrices. However, using the fact that $U^{-1}(t) = V(t)$, $c_1(t)$ can be calculated as

$$c(t) = U^{-1}(t)b(t) = V(t)b(t) \tag{2.20}$$

or

$$\begin{pmatrix} c_1(t) \\ c_2(t) \\ \vdots \\ c_n(t) \end{pmatrix} = \begin{pmatrix} v_1^T(t) \\ v_2^T(t) \\ \vdots \\ v_n^T(t) \end{pmatrix} \cdot b(t) \tag{2.21}$$

The scalar $c_1(t)$ can be expressed from (2.21) as

$$c_1(t) = v_1^T(t) \cdot b(t) \tag{2.22}$$

where $v_1(t)$ is an oscillatory eigen mode of the adjoint system $\dot{y} = -A^T(t)y$ corresponding to Equation (2.5). Equation (2.22) implies that $c_1(t)$ is an orthogonal projection of the perturbation vector $b(t)$ onto $v_1^T(t)$. This is an expected result, as from the bi-orthogonality condition of $v_i(t)$ and $u_j(t)$, it follows that the oscillatory eigen mode of the adjoint system $v_1(t)$ is orthogonal to all of the decaying modes $u_i(t),\ i = 2, \ldots, n$ of the original system (2.5) [10]. Thus there is no need to calculate any other $T$-periodic eigen modes other than $v_1(t)$. The $i^{th}$ coordinate of $v_1(t)$, $i = 1, \ldots, n$ is a measure of how much of a perturbation of the $i^{th}$ equation of the system ($i^{th}$ coordinate of $b(t)$) at time $t$ will be projected into phase deviation. Therefore, a set of $n$ $T$-vectors $v_1$ is referred to as the *perturbation projection vectors* (PPV) of the system.

The monodromy matrix of the adjoint system $\Omega$ can be written in terms of $\Phi$, the monodromy matrix of the original system as

$$\Omega(t, t+T) = \Phi^T(t+T, t) \tag{2.23}$$

The vector $v_1(t)$ for each time $t \in [0, T)$ can be extracted from $\Omega(t-T, t)$ by doing an eigenvalue decomposition. However there are more efficient ways of calculating $v_1(t)$ [8] that will be described in Sections 2.4.1 and 2.4.2.

An analysis similar to the ones performed for ODEs in Sections 2.2, 2.3 and above, can be carried out for the following LPTV system of differential-algebraic equations (DAEs) as well [8]:

$$\frac{d}{dt}(C(t)x) + G(t)x = 0 \tag{2.24}$$

The linear system (2.24) is obtained by linearization of

$$\frac{d}{dt}q(x) + g(x) + u = 0 \tag{2.25}$$

around the PSS solution, where $q(x)$ represents the charges (fluxes) of capacitors (inductors), $g(x)$ represents the currents through resistive components, and $u$ represents the independent current and voltage sources. The matrices $G(t)$ and $C(t)$ from (2.24) are obtained as

$$G(t) = \frac{d}{dx} g(x)\Big|_{x=x_s} \tag{2.26}$$

and

$$C(t) = \frac{d}{dx} q(x)\Big|_{x=x_s} \tag{2.27}$$

where $x_s$ is a periodic solution of the autonomous system of DAEs (2.25). These systems are obtained from autonomous circuits, such as oscillators.

### 2.4.1. Time-Domain Algorithm for PPV Calculation

An algorithm for calculation of $v_1(t)$, based on a linearization of the time-domain PSS solution of an oscillator consists of the following steps:

1. Calculate the large-signal PSS solution $x_s(t), t \in [0, T)$ of an oscillator described by (2.25) using a time-domain technique, such as the shooting method or the finite-difference method [3]. Save the matrices $G(t)$ and $C(t)$ that form the linear model of the oscillator (2.24), linearized around the PSS solution.

2. Calculate the monodromy matrix $\Omega(0, T)$ of the adjoint system given by $C^T(t)dy/dt - G^T(t)y = 0$. To do this, calculate the state transition matrix $\Omega(t, T)$ by numerically integrating the adjoint system backwards in time starting from the initial condition $\Omega(T, T) = I_n$, to time $t = 0$. The state transition matrix $\Omega(t, T)$ evaluated at time $t = 0$ is the monodromy matrix $\Omega(0, T)$. Note that integration backwards in time is used because the

characteristic exponents of the adjoint system are negative of the characteristic exponents of the original system. Also, the characteristic multipliers of the adjoint system are reciprocals of the characteristic multipliers of the original system. This means that decaying eigen modes of the original system correspond to unstable eigen modes of the adjoint system: $\lambda_i > 1$, $i = 2, \ldots n$. Therefore, integration of the adjoint system forward in time is not numerically stable.

3. Calculate the oscillatory eigen mode $u_1(T)$ of the original system (2.24) as $u_1(T) = \dot{x}_s(T)$. The derivative $\dot{x}_s(t)$ points in the direction of the tangent to the orbit of the oscillator and any small perturbation in that direction will result only in a phase deviation, without changing the orbit itself. Therefore, $\dot{x}_s(T)$ can be chosen to be an oscillatory eigenvector at time $T$.

4. Calculate $v_1(T)$ by computing the oscillatory eigenvector of $\Omega(0, T)$ corresponding to the oscillatory eigenvalue $\lambda_1 = 1$. Scale $v_1(T)$ to satisfy $v_1^T(T)C(T)u_1(T) = 1$. If it is difficult to distinguish the oscillatory eigen mode among several nearly oscillatory eigen modes $\lambda_i \approx 1$, then choose the eigenvector which points more than others in the direction of $C(T)\dot{x}_s(T)$, i.e., the one which has the largest inner product with $C(T)\dot{x}_s(T)$.

5. Calculate $v_1(t)$ along a PSS period, $t \in (0, T]$. To do this, integrate the adjoint system starting from an initial condition $v_1(T)$ at time $T$ backwards in time to $t = 0$. The reason for integration backwards in time is the same as in Step 2.

The algorithm for calculation of $v_1(t)$, based on a linearization of the time-domain PSS solution of an oscillator is illustrated in Figure 2.7.

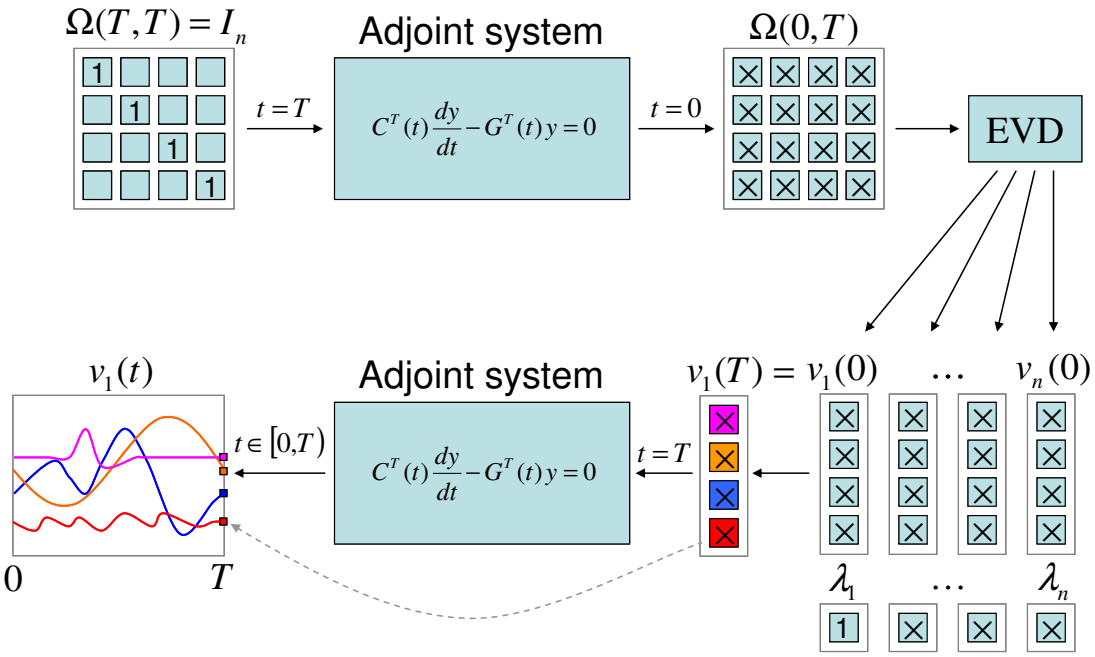


Figure 2.7. Block diagram of the time-domain algorithm for PPV calculation.

### 2.4.2. Frequency-Domain Algorithm for PPV Calculation

Instead of going directly to the algorithm for calculating $v_1(t)$, let us first define the problem in the frequency domain. The frequency-domain formulation of the autonomous system of DAEs (2.25) is represented as

$$\Omega q_f(X) + g_f(X) + u_f = 0 \tag{2.28}$$

where $\Omega$ represents the derivative operator in the frequency domain (do not confuse with the notation used for the monodromy matrix of the adjoint system), $q_f(X)$ represents the Fourier coefficients of charges (fluxes) of capacitors (inductors), $g_f(X)$ represents the currents of resistors in terms of their Fourier coefficients, and $u_f$ represents the Fourier coefficients of the independent current and voltage sources. $X = \Gamma x$ is the set of Fourier coefficients of all circuit unknowns, and $\Gamma$ is a Fourier transform matrix operator that maps the time-domain wave-

form into the frequency-domain spectrum. Linearization of (2.28) results in the frequency-domain Jacobian matrix

$$J = \Big[ J_{ij} \Big], \qquad i, j = 1, \ldots, n \tag{2.29}$$

where $J_{ij}$ is a $K \times K$ matrix, and K is the number of Fourier coefficients that represent a single variable. Block $J_{ij}$ contains the sensitivities of all the Fourier coefficients of the $i^{th}$ equation of (2.25) with respect to all the Fourier coefficients of the $j^{th}$ unknown of (2.25). $J_{ij}$ is defined in terms of $G$ and $C$ as follows:

$$J_{ij} = \Gamma G_{ij}(t) \Gamma^{-1} + \Omega \Gamma C_{ij}(t) \Gamma^{-1} \tag{2.30}$$

where $G_{ij}(t)$ and $C_{ij}(t)$ are $T$-vectors that correspond to $dg_i(x)/dx_j$ and $dq_i(x)/dx_j$, from (2.26) and (2.27) at each time point along the period of the PSS solution.

An algorithm for calculation of $v_1(t)$, based on a linearization of the frequency-domain PSS solution of an oscillator is summarized:

1. Calculate the large-signal frequency domain PSS solution $X_s$ of an oscillator described by (2.28). Save the Jacobian matrix $J$ at the solution point. Transform $X_s$ into time domain waveforms $x_s(t)$. Save $C(0) = dq(x)/dx,\ x = x_s(0)$, as available from the time-domain evaluations of the nonlinearities.

2. Calculate $u_1(0) = \dot{x}_s(0)$, where the time-derivative of the PSS solution $\dot{x}_s(t)$ is calculated analytically in the frequency domain $\dot{x}_s(t) = \Gamma^{-1} \Omega X_s$.

3. Calculate the null space of the transposed Jacobian matrix by doing a singular value decomposition and choosing the right singular vector corresponding to the singular value 0. The null space of $J^T$ is the frequency-domain representation of $v_1(t)$, $V_1 = null(J^T)$. Convert $V_1$ into the time domain, $v_1(t) = \Gamma^{-1} V_1$. Scale $v_1(t)$ to satisfy $v_1^T(0) C(0) u_1(0) = 1$.

The algorithm for calculation of $v_1(t)$, based on a linearization of the frequency-domain PSS solution of an oscillator is illustrated in Figure 2.8.

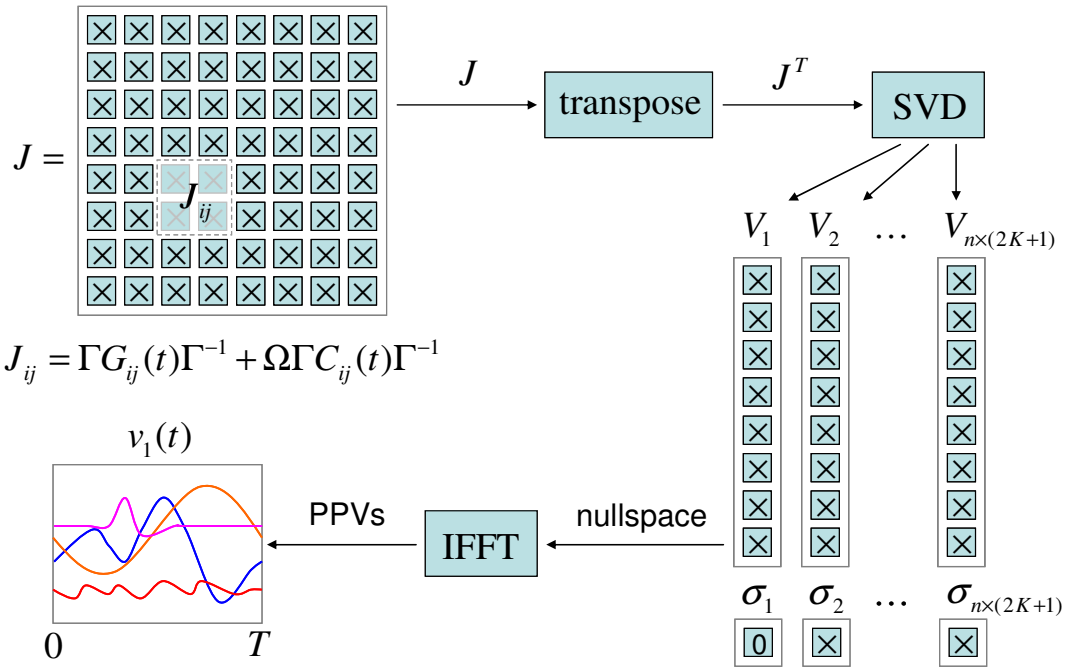


Figure 2.8. Block diagram of the frequency-domain algorithm for PPV calculation.

## 2.5. Calculation of Phase Noise

Once the perturbation projection vectors $v_1(t)$ have been determined, a single-sideband noise spectral density $\mathcal{L}(f_m)$ can be calculated as [4]

$$\mathcal{L}(f_m) = 10log_{10}\frac{f_{osc}^2 c(f_m)}{\pi^2 f_{osc}^4 c^2(f_m) + f_m^2} \tag{2.31}$$

The frequency of oscillation $f_{osc}$ is known from the underlying PSS analysis, and the scalar noise constant $c(f_m)$ is calculated as a sum of two components:

$$c(f_m) = c_w + c_c(f_m) \tag{2.32}$$

where $c_w$ represents the frequency-independent contribution of all white noise sources, and $c_c(f_m)$ is the contribution of all colored noise sources at the offset

frequency frequency $f_m$. If there are $p_w$ white and $p_c$ colored noise sources in the circuit, then the constants $c_w$ and $c_c(f_m)$ can be calculated [4] as

$$c_w = \sum_{i=1}^{p_w} c_{wi} = \sum_{i=1}^{p_w} \int_0^T \left( v_1^T(\tau) b_{wi}(x_s(\tau)) \right)^2 dt \tag{2.33}$$

and

$$c_c(f_m) = \sum_{i=1}^{p_c} c_{ci}(f_m) = \sum_{i=1}^{p_c} \int_0^T \left( v_1^T(\tau) b_{ci}(x_s(\tau), f_m) \right)^2 dt \tag{2.34}$$

where $b_{wi}(x_s(\tau))$ maps the $i^{th}$ white noise source to the equations of system (2.25), $b_{wi}(x_s(\tau), f_m)$ maps the $i^{th}$ colored noise source at the offset frequency $f_m$ to the equations of system (2.25). The noise sources are calculated given the bias conditions corresponding to the PSS solution $x_s(t)$ at time $t = \tau$. A practical implementation and structure of the noise matrices are well illustrated in [11].

## 2.6. Implementation Notes

Phase noise analyses based on the frequency-domain harmonic balance method and the time-domain shooting method were implemented in our in-house version of SPICE3, a general purpose analog circuit simulator.

As shown in Section 3.2.1, the SVD computation is the primary contributor to the overall phase noise computation time in the frequency-domain method. The accuracy of the PPVs and phase noise is directly related to the accuracy of harmonic balance Jacobian null space, which is calculated using the SVD. Therefore, while choosing an SVD algorithm, not only its speed but also its accuracy should be taken into consideration.

Currently, there are two SVD algorithms which are better than others in terms of speed, i.e., variations of the *QR-iteration* and the *divide-and-conquer* algorithm [12]. In terms of speed, the divide-and-conquer algorithm is more efficient compared to the QR-iteration when working with dense matrices larger

than $25 \times 25$. Harmonic balance matrices that rise from practical problems are much larger than this size but are generally sparse. These algorithms including all other SVD algorithms are iterative [13], and they have different properties. The QR-iteration finds all the singular values with a high relative accuracy, whereas the divide-and-conquer algorithm finds the singular values with a high absolute accuracy. Our goal is to obtain the right singular vector that corresponds to the smallest singular value. Therefore, relative accuracy is of higher priority in phase noise calculations.

To make a proper choice of the SVD algorithm, speed and accuracy of two LAPACK [14] SVD solvers were compared. The first solver is an implementation of the QR-iteration algorithm, and it is accessed through the DGESVD driver routine. The second solver is an implementation of the divide-and-conquer algorithm, and it is accessed through the DGESDD driver routine [15].

The phase noise of a three-stage ring oscillator (see Section 3.1.1) was calculated using both the DGESVD and DGESDD SVD solvers. A colored noise constant at 1kHz offset frequency was chosen to be a figure of merit while comparing the two SVD solvers. As we can see from Figure 2.9, the SVD algorithm does not have a significant effect on the accuracy of the phase noise constant. Table 2.1 shows that the phase noise constants calculated using the two different SVD solvers are practically indistinguishable from each other. In Table 2.1 $N_{harm}$ is the number of harmonics, $J_{size}$ is the size of the harmonic balance Jacobian matrix, $\varepsilon_{abs}$ is the difference between the phase noise constants calculated using the different SVD solvers.

Figure 2.10 shows that it takes less time for the divide-and-conquer SVD solver to perform an SVD of the harmonic balance Jacobian matrices of practical sizes.

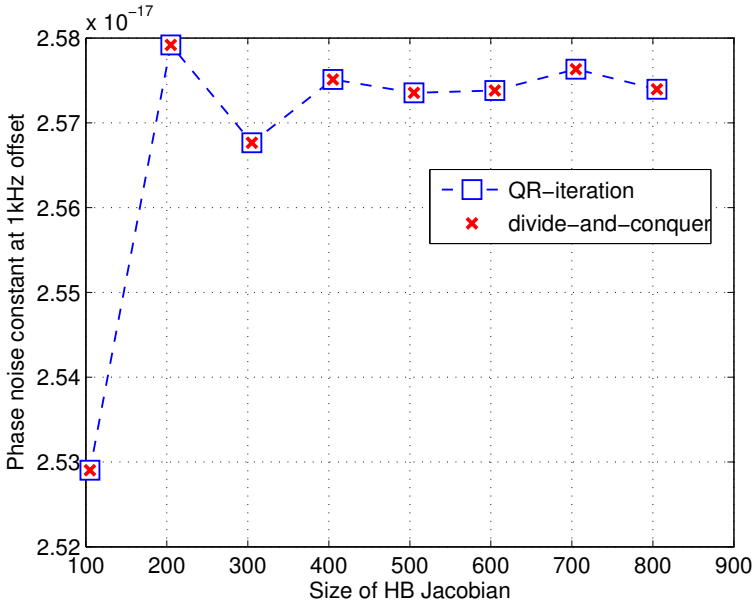


Figure 2.9. Phase noise constants calculated using different SVD solvers.

| $N_{harm}$ | $J_{size}$ | $\varepsilon_{abs}$ |
|---|---|---|
| 10 | 105 | $+1.85 \times 10^{-32}$ |
| 20 | 205 | $-1.79 \times 10^{-31}$ |
| 30 | 305 | $-9.18 \times 10^{-31}$ |
| 40 | 405 | $-2.10 \times 10^{-31}$ |
| 50 | 505 | $+2.13 \times 10^{-31}$ |
| 60 | 605 | $-3.39 \times 10^{-31}$ |
| 70 | 705 | $-1.27 \times 10^{-30}$ |
| 80 | 805 | $+6.04 \times 10^{-31}$ |

Table 2.1. Difference between phase noise constants.

While showing a comparable accuracy in SVD computation for a given problem, the divide-and-conquer based solver shows better speed performance compared to the QR-iteration based one. Therefore, for this work the DGESDD

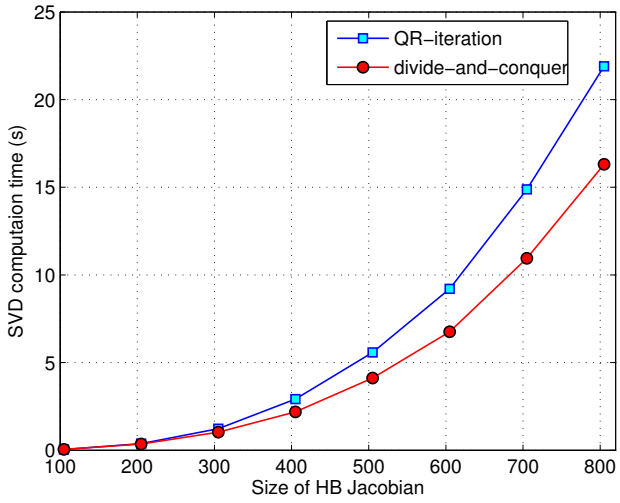


Figure 2.10. SVD computation speed using different SVD solvers.

driver based on the divide-and-conquer algorithm was chosen for calculation of the null space of the harmonic balance Jacobian matrix.

# 3. SIMULATION RESULTS AND COMPARATIVE ANALYSIS

A set of test oscillator circuits were simulated to compare the frequency-domain and time-domain phase noise analyses. The frequency-domain analysis that was implemented during this work, is based on the harmonic balance method available in our in-house version of the SPICE3 simulator [16], [17]. The time-domain phase noise analysis is based on the time-domain PSS solution. The original analysis was implemented to work with data obtained from a transient analysis that was run for a sufficiently long time [11]. This analysis was modified to work in conjunction with the shooting method, also available in our version of SPICE3 [16].

This chapter presents results and comparisons of phase noise and PPV simulation for three oscillator circuits using the time-domain and the frequency-domain techniques. The simulated oscillators are a three-stage ring oscillator, NMOS cross-coupled oscillator, and a Colpitts oscillator.

## 3.1. Phase Noise and PPV Calculations

Simple level-one models [18] and the more accurate and complex BSIM3 models [19] were used to model MOS transistors in the oscillator circuits. Sections 3.1.1, 3.1.2 and 3.1.3 present and explain in detail the phase noise and the PPVs calculated using the level-one models. Phase noise and the PPVs obtained using the BSIM3 models are presented in Section 3.1.4

### 3.1.1. Three-Stage Ring Oscillator

A three-stage ring oscillator circuit is shown in Figure 3.1. The transistor sizes and capacitor values are identical for each of the three inverters in the ring oscillator. The frequency of oscillation is 435.8MHz.

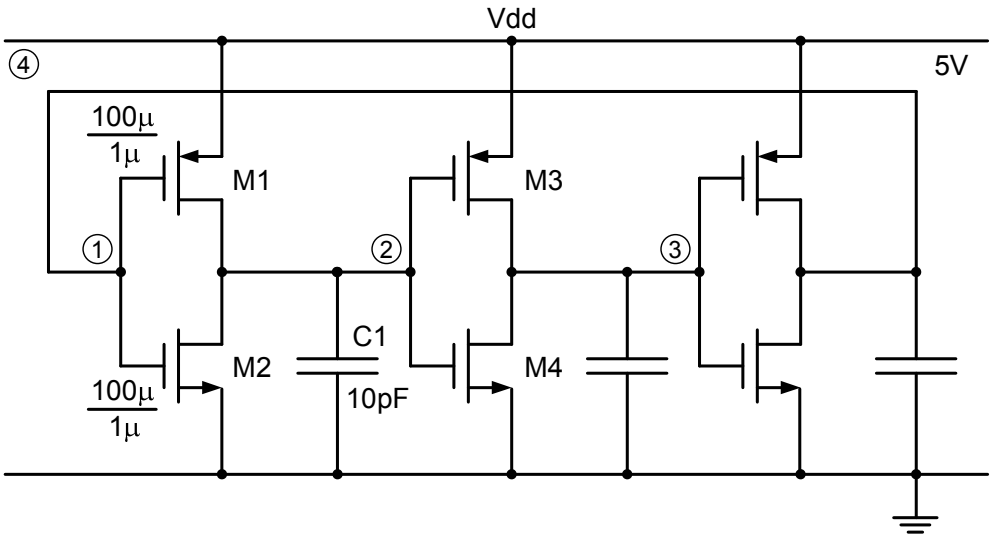


Figure 3.1. Schematic of a three-stage ring oscillator.

There are 5 unknowns in the mathematical model of this circuit, and its behavior is modeled by 5 equations, each corresponding to a certain physical law. The circuit unknowns are the node voltages and the current through the power supply voltage source $Vdd$. This formulation is known as the modified nodal analysis (MNA) [20]. Table 3.1 shows the physical laws with their equation units and the circuit unknowns.

| **equation : unit** | **unknown** |
|---|---|
| KCL at node 1 : current | $v_1$ |
| KCL at node 2 : current | $v_2$ |
| KCL at node 3 : current | $v_3$ |
| KCL at node 4 : current | $v_4$ |
| BCE for $Vdd$ : voltage | $i_{Vdd}$ |

Table 3.1. Equations and unknowns of the three-stage ring oscillator circuit.

For a PSS simulation with the time-domain Newton's shooting method, a fine time discretization of about 1000 time points per period was used. For

the harmonic balance method, the signals were approximated by a truncated Fourier series with 81 nonzero coefficients, i.e., a DC component and coefficients of sines and cosines at 40 distinct frequencies that are multiples of the oscillation frequency. Tight absolute and relative tolerances ($\varepsilon_{abs} = 10^{-12}$ and $\varepsilon_{rel} = 10^{-7}$) were applied to the convergence criteria for Newton's method.

Two families of PPV waveforms are shown in Figure 3.2. In this figure

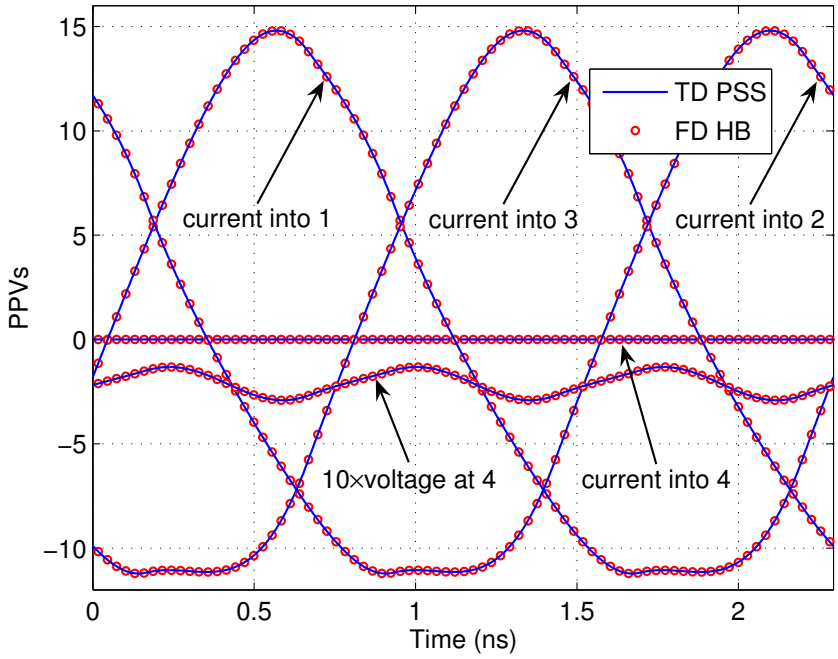


Figure 3.2. PPVs of the three-stage ring oscillator.

and in the following figures, results obtained based on the time-domain PSS and frequency-domain harmonic balance are marked as *TD PSS* and *FD HB*, respectively. The PPVs are in good agreement.

Each PPV provides information of an oscillator's phase sensitivity to perturbation of certain signals in the circuit at any time along a period of the steady-state. These signals can be determined from the circuit's equations. The units of the equations help to verify the nature of the signals. In our example of the ring oscillator, four PPVs project a perturbation of current to phase deviation

and one PPV projects a perturbation of voltage to phase deviation. For example, the PPV that corresponds to the first circuit equation, i.e., KCL at node 1 (see Table 3.1), depicts how sensitive the phase is to the injection of extra current into node 1, or equivalently, to perturbation of any of $M1$ and $M2$ gate currents $i_{g1}$, $i_{g2}$, $M3$ and $M4$ drain currents $i_{d3}$, $i_{gd4}$ and the capacitor current $i_{C1}$. The $5^{th}$ PPV corresponds to the branch constitutive equation (BCE) for $Vdd$ and shows the sensitivity of the phase to the changes in the power supply voltage, or to perturbations of $v_4$ or $v_{ground}$.

As expected, the PPVs in Figure 3.2 are periodic vectors. The PPVs of KCLs at nodes 1, 2 and 3 are $\pm 2\pi/3$ phase shifted copies of each other, as there is $\pm 2\pi/3$ delay between the three inverters. Positive peaks of these PPVs occur when inverters switch from high to low, and negative peaks occur when inverters switch from low to high. This is an expected result as the phase of the circuit is more sensitive to signal perturbations during transitions. The phase is not sensitive to current injection into node 4 as voltage $v_4$ is supplied by an ideal (with zero resistance) voltage source $Vdd$, and therefore, any extra current injected into node 4 is shorted to ground and does not affect the circuit. The PPV of the BCE for $Vdd$ was scaled up by 10 times for a clear visual demonstration. It is a periodic signal at $3f_{osc}$, where 3 is the number of stages. It is always negative implying that a positive impulse in $v_4$ always shifts the circuit waveforms backwards in time relative to the waveforms of the unperturbed oscillator.

The phase noise spectrum $S_{\mathcal{L}}(f)$ of the oscillator is shown in Figure 3.3. The phase noise calculated using the time-domain and the frequency-domain techniques are in good agreement. The transistor noise model includes both thermal and flicker noise information. It can be seen from Figure 3.3 that at small offset frequencies where flicker noise dominates, the slope of the phase noise spectrum

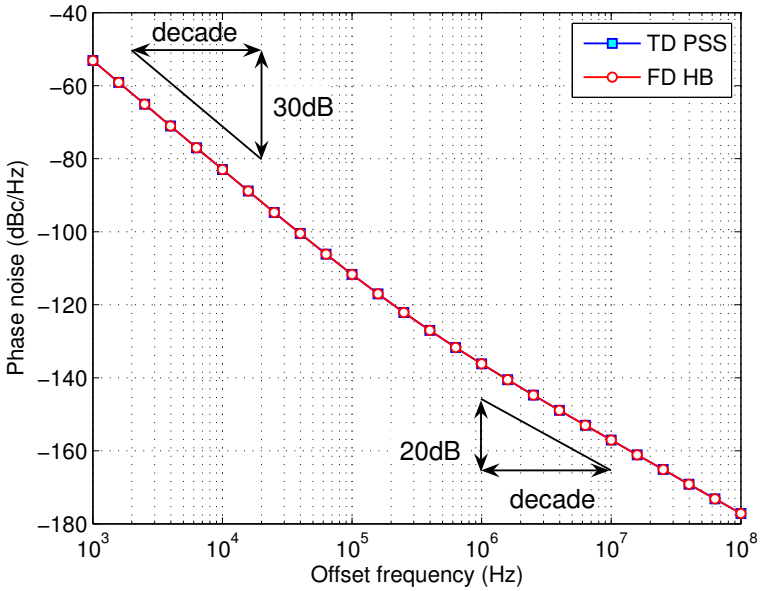


Figure 3.3. Phase noise of the three-stage ring oscillator.

is -30dB/dec. At high offset frequencies the slope of the spectrum is -20dB/dec, because white noise is dominant in that region.

### 3.1.2. NMOS Cross-Coupled Oscillator

The schematic of an NMOS cross-coupled oscillator is shown in Figure 3.4. The circuit was analyzed in our version of SPICE3. The oscillation frequency is 2.37GHz.

The circuit operation is described by 9 physical laws in terms of 9 circuit unknowns which are listed in Table 3.2.

The PPVs of the cross-coupled oscillator obtained using the harmonic balance information in the periodic steady state are in good agreement with the PPVs calculated based on the time-domain PSS solution. The PPVs that project perturbations in 9 circuit equations to the phase of the oscillator circuit are presented in Figure 3.5.

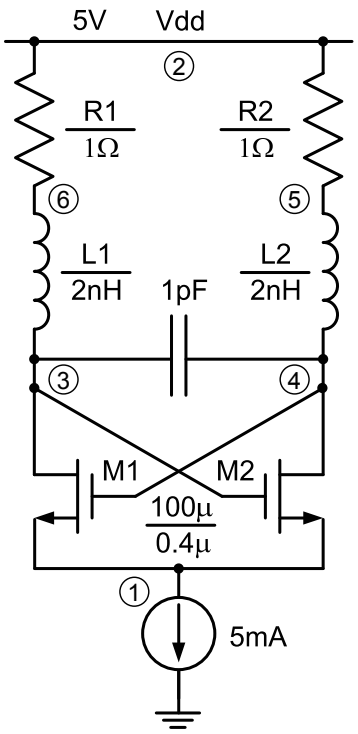


Figure 3.4. Schematic of an NMOS cross-coupled oscillator.

| **equation** : **unit** | **unknown** |
|---|---|
| KCL at node 1 : current | $v_1$ |
| KCL at node 2 : current | $v_2$ |
| KCL at node 3 : current | $v_3$ |
| KCL at node 4 : current | $v_4$ |
| KCL at node 5 : current | $v_5$ |
| KCL at node 6 : current | $v_6$ |
| BCE for $L1$ : voltage | $i_{L1}$ |
| BCE for $L2$ : voltage | $i_{L2}$ |
| BCE for $Vdd$ : voltage | $i_{Vdd}$ |

Table 3.2. Equations and unknowns of the NMOS cross-coupled oscillator circuit.

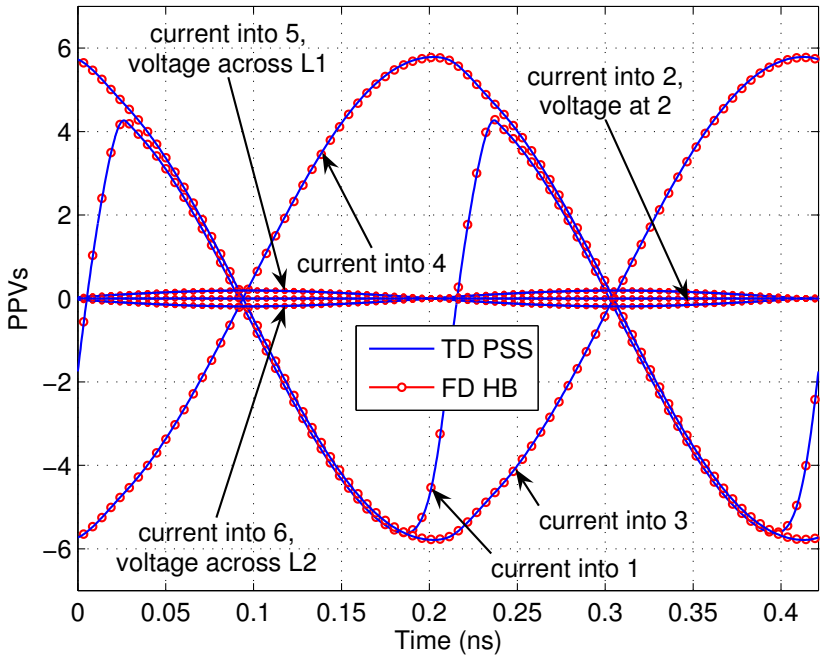


Figure 3.5. PPVs of the NMOS cross-coupled oscillator.

There are three pairs of PPVs that look symmetric around the abscissa axis, i.e., the PPVs of $i_3$ and $i_4$, $i_5$ and $i_6$, $v_{L1}$ and $v_{L2}$. In fact, they are 180° shifted replicas of each other. This observation is explained by the symmetric topology and the differential operation of the circuit. Therefore, there is a 180° phase shift between the signals in the left and right half's of the circuit. There is a ±90° phase difference between the PPVs of currents into the capacitor terminal and the PPVs of the voltages across the inductors, as the energy storing signals of the capacitor and inductors themselves differ from each other by ±90°.

There are two pairs of overlapping PPVs, like the PPV of current into node 5 and the PPV of voltage across $L1$. Though, these PPVs are related to signals of different nature, they are of the same amplitude. This is because any positive perturbation $+\Delta v_{L1}$ decreases both $v_{R1}$ and $i_{R1}$ by the same amount $-\Delta v_{R1} = -\Delta i_{R1}$, as $R1 = 1\Omega$. The perturbation $-\Delta i_{R1}$ in the left branch of the

circuit causes $+\Delta i_{R2}$ response in the right branch, which is equivalent to injection of $+\Delta i_5 = +\Delta i_{R2} = +\Delta v_{L1}$ current into node 5. The same effect of perturbations $+\Delta i_6$ and $\Delta v_{L2}$ on phase can be explained in a similar way.

Those PPVs that do not have a pair, correspond to KCLs at common nodes 1 and 2, and the BCE for $Vdd$, can not be related to any half of the circuit. These PPVs are either constants or periodic vectors at $2f_{osc}$ like the PPV corresponding to KCL at node 1. The phase of the circuit signals is not sensitive either to injection of current into node 2, or to perturbation of voltage at node 2. The first is true, because any extra current injected into node 2 is shorted to ground through the ideal voltage source $Vdd$. The second can be explained as follows. The ideal current source does not fix the voltage at node 1. It is defined by the rest of the circuit, so whenever there is a perturbation of $v_2$, voltage $v_1$ follows it to keep $v_2 - v_1$ constant. Therefore, a perturbation of $v_2$ affects only amplitudes of all the voltages in the circuit and it does not affect the phase. If the ideal current source is replaced by a real source with a finite resistance, such as an NMOS transistor tail current source, as in Figure 3.6, the PPV corresponding to the perturbation of the voltage at node 2 will differ from zero, as shown in Figure 3.7. This PPV can be used to estimate the sensitivity of the oscillator's phase noise to the power supply noise [21].

The phase noise spectrum $S_{\mathcal{L}}(f)$ of the cross-coupled oscillator is shown in Figure 3.8. The spectrum obtained using the frequency-domain harmonic balance based analysis is in good agreement with the spectrum calculated using the time-domain based technique. The phase noise of the circuit is affected both by flicker and thermal noise sources. This can be seen from the phase noise spectrum plot as it has slopes of -30dB/dec and -20dB/dec at low and high offset frequencies, respectively. This NMOS cross-coupled oscillator has a lower $1/f^3$ corner frequency

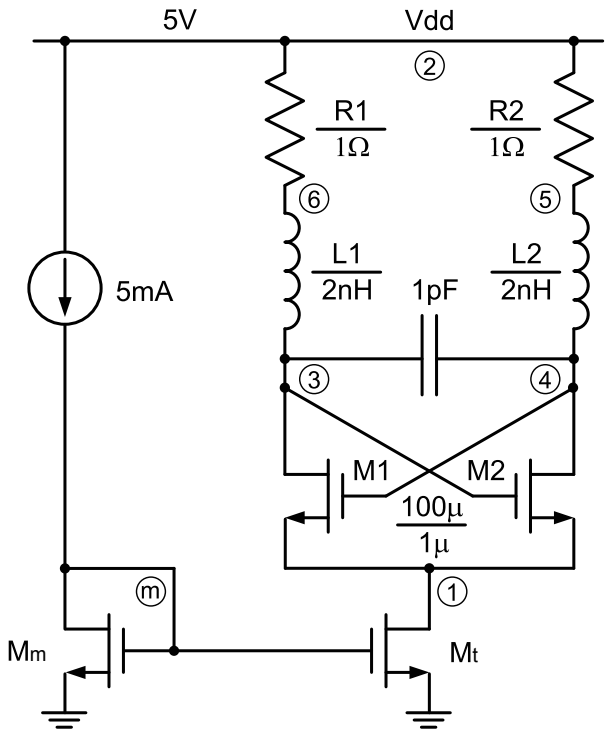


Figure 3.6. An NMOS cross-coupled oscillator with a transistor tail current source.

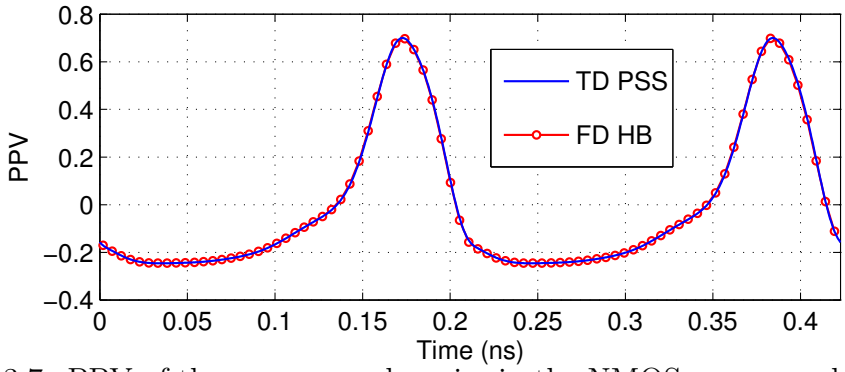


Figure 3.7. PPV of the power supply noise in the NMOS cross-coupled oscillator with transistor tail current source.

of about 10kHz compared to about 200kHz in our previous example (three-stage ring oscillator).

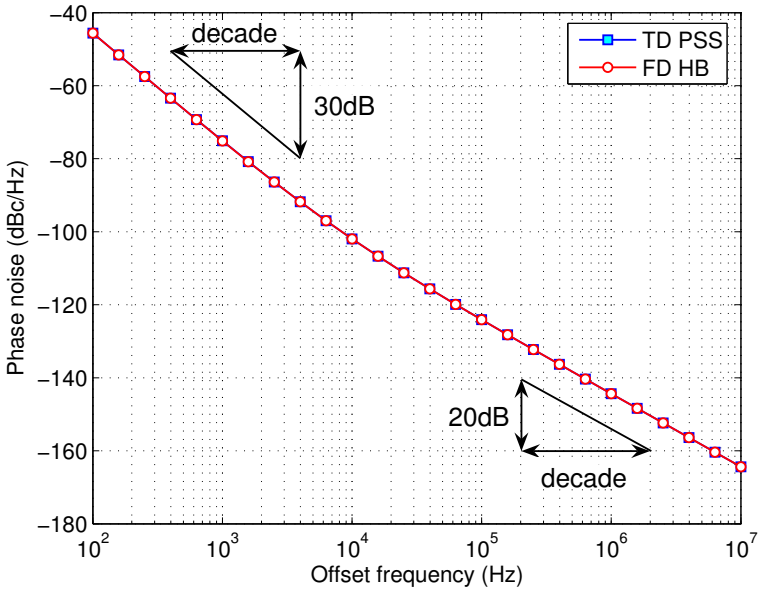


Figure 3.8. Phase noise of the NMOS cross-coupled oscillator.

### 3.1.3. Colpitts Oscillator

Figure 3.9 shows the schematic of a Colpitts oscillator and Table 3.3 shows its 7 circuit equations and 7 circuit unknowns.

| **equation : unit** | **unknown** |
|---|---|
| KCL at node 1 : current | $v_1$ |
| KCL at node 2 : current | $v_2$ |
| KCL at node 3 : current | $v_3$ |
| KCL at node 4 : current | $v_4$ |
| BCE for $L1$ : voltage | $i_{L1}$ |
| BCE for $Vbias$ : voltage | $i_{Vbias}$ |
| BCE for $Vdd$ : voltage | $i_{Vdd}$ |

Table 3.3. Equations and unknowns of the Colpitts oscillator circuit.

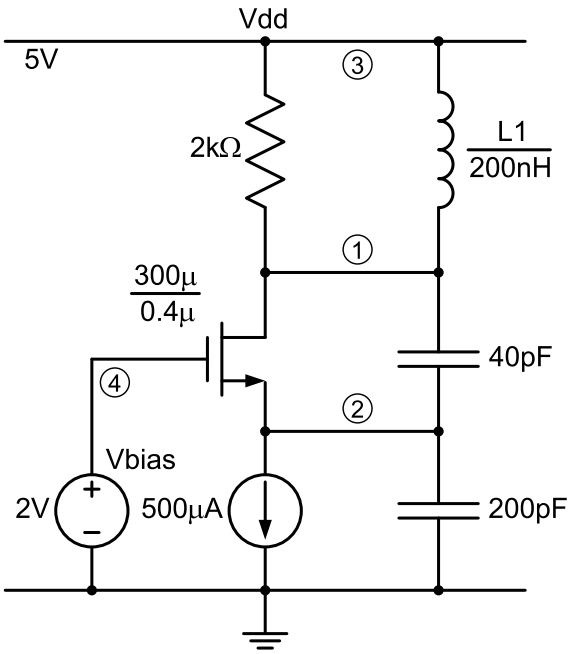


Figure 3.9. Schematic of a Colpitts oscillator.

The oscillator provides an output signal at a frequency of 61.6MHz. As we can see from Figure 3.10, the PPVs are in good agreement.

The PPVs that are related to voltages in the BCEs for $L1$, $Vbias$ and $Vdd$ are scaled up by 20 times. From the figure we can observe that the phase of the oscillator is more sensitive to injection of extra current into node 1 than into node 2. The PPV of the power supply voltage at node 3 and the PPV of voltage across $L1$ are mirror images of each other, as a positive perturbation of voltage at node 3 will cause the tank to charge, and a positive perturbation of the voltage across $L1$ will cause the tank to discharge.

To understand the shape of the PPV of the gate voltage $v_4$, let us look at Figure 3.11, where the transistor drain current and the tank voltage waveforms are shown. The PPV of $v_4$ is close to zero only inside the time interval where the drain current is low and around the point where the PPV crosses the abscissa axis. In the first half of the period the sign of the PPV changes from negative to positive

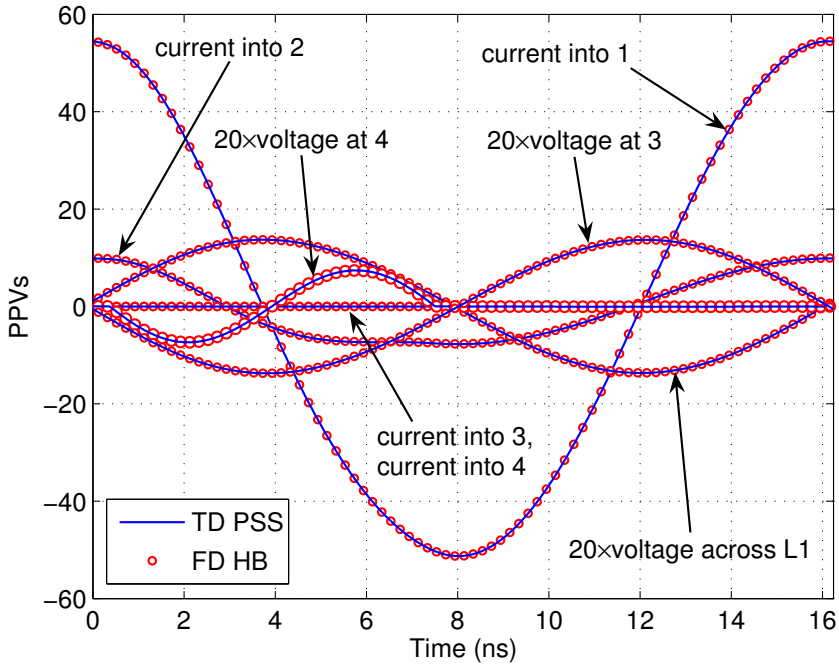


Figure 3.10. PPVs of the Colpitts oscillator.

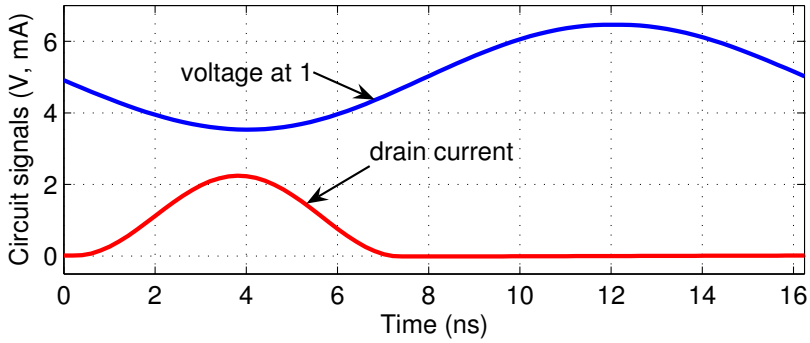


Figure 3.11. Voltage $v_1$ and current $i_d$ of the Colpitts oscillator.

as the tank voltage slope changes from negative to positive. The point where the PPV crosses zero corresponds to the extremum point of the tank amplitude where any perturbation of $v_4$ will project only into amplitude noise. Note that at the moment when the drain current peaks and the transistor $1/f$ noise is high, the phase is not sensitive to current injections into nodes 1 and 2. This improves the phase noise performance of the Colpitts oscillator [1] (see Figure 3.12).

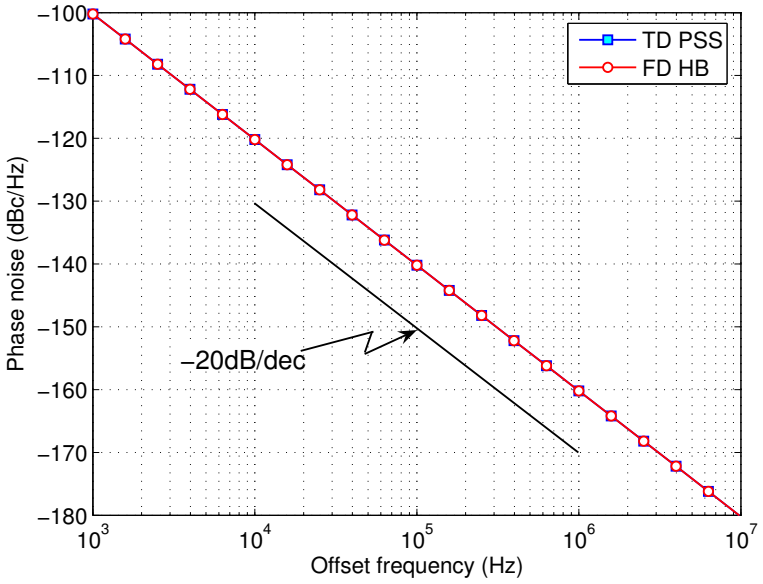


Figure 3.12. Phase noise of the Colpitts oscillator.

Indeed, for the given example, the phase noise at 1kHz offset frequency is as low as -100dBc/Hz. Note that most of the transistor flicker noise was projected into amplitude noise, and there are no other colored noise sources in the circuit. The thermal noise of the 2kΩ resistor is the primary contributor to the oscillator's phase noise, which can be seen from the phase noise plot. The slope of the phase noise spectrum is -20dB/dec at any offset frequency, indicating that thermal noise is dominant at any offset frequency.

### 3.1.4. Calculations with BSIM3 Models

The BSIM3 model was used for calculation of the PPVs and the phase noise of the oscillators from the previous sections. The PPVs and the phase noise obtained using the BSIM3 model are presented in this section, and they generally do not match the results obtained using level-one models. This is because these models reflect the behavior of the transistors fabricated in a different process.

Figure 3.13 shows the PPVs of the three-stage ring oscillator from Section 3.1.1. Figure 3.14 shows the phase noise of the ring oscillator. The PPVs

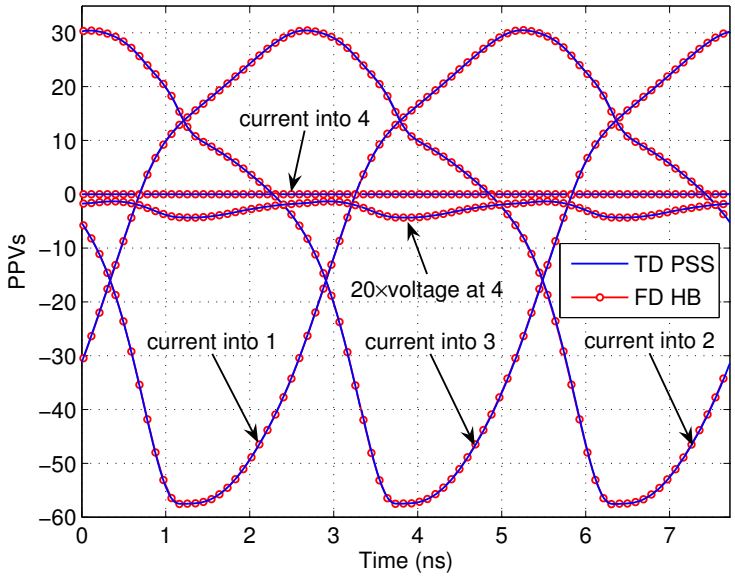


Figure 3.13. PPVs of the three-stage ring oscillator with the BSIM3 MOSFET model.

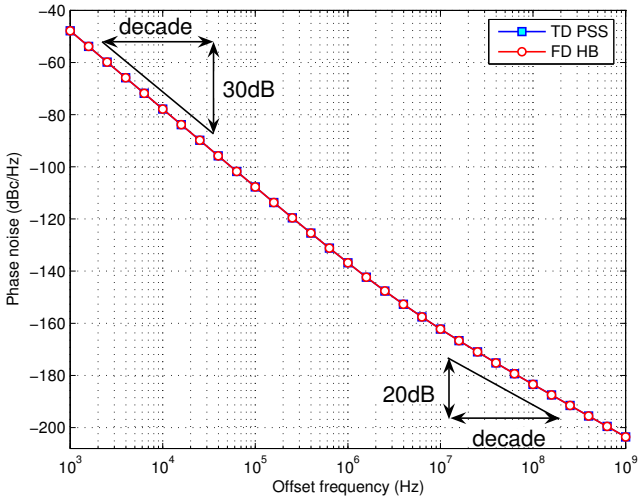


Figure 3.14. Phase noise of the three-stage ring oscillator with the BSIM3 MOSFET model.

and the phase noise obtained using the time-domain and the frequency-domain methods are in good agreement.

Figure 3.15 shows the PPVs of the NMOS cross-coupled oscillator presented in Section 3.1.2. The phase noise of the oscillator is presented in Figure 3.16.

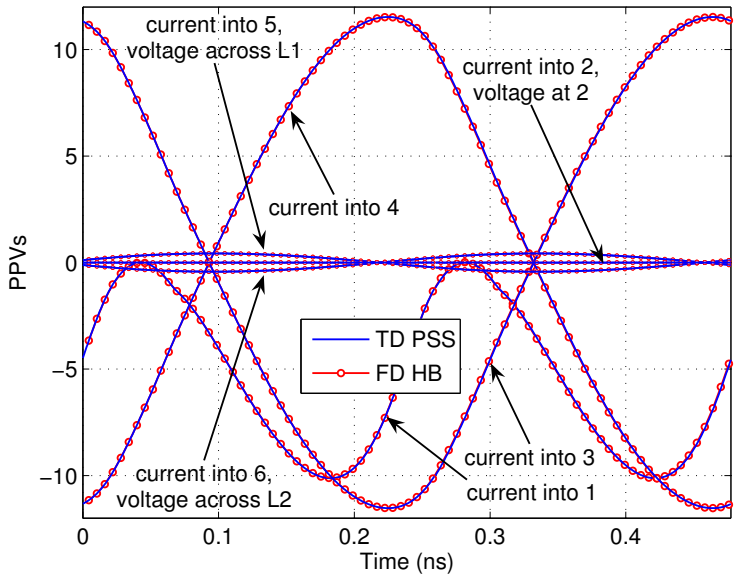


Figure 3.15. PPVs of the NMOS cross-coupled oscillator with the BSIM3 MOSFET model.

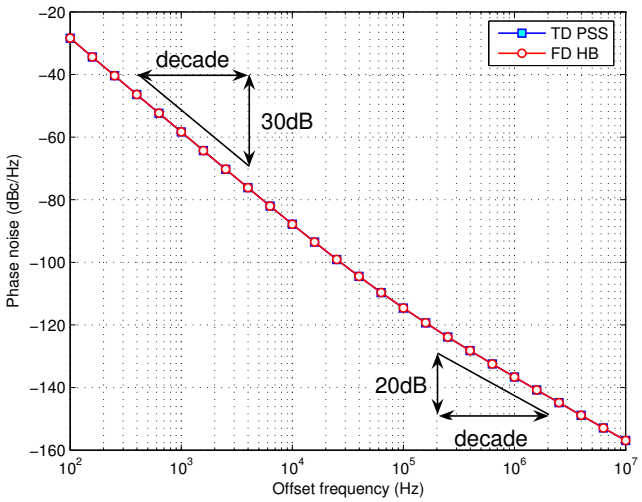


Figure 3.16. Phase noise of the NMOS cross-coupled oscillator with the BSIM3 MOSFET model.

The PPVs and the phase noise obtained using different techniques are in good agreement.

The PPVs and the phase noise of the Colpitts oscillator from Section 3.1.3 are shown in Figures 3.17 and 3.18, respectively. The results obtained using the

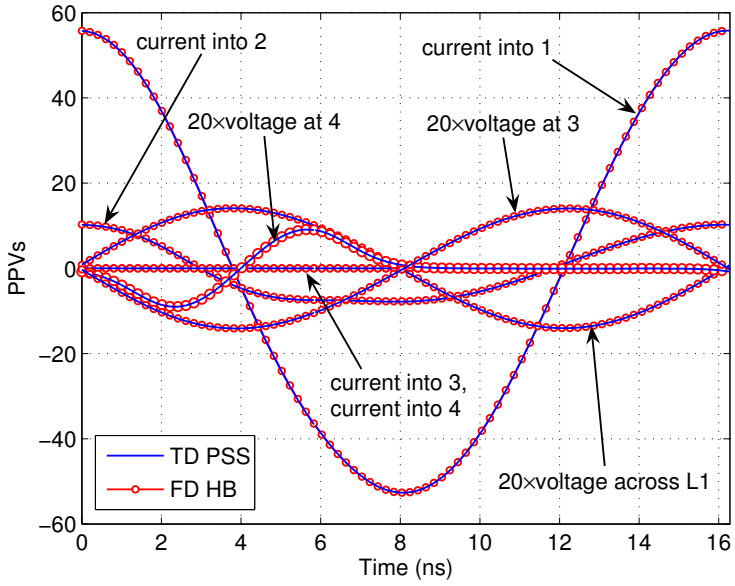


Figure 3.17. PPVs of the Colpitts oscillator with the BSIM3 MOSFET model.

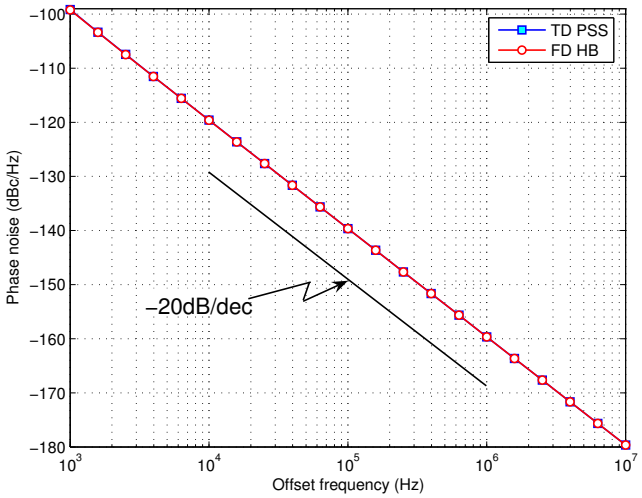


Figure 3.18. Phase noise of the Colpitts oscillator with the BSIM3 MOSFET model.

time-domain and the frequency-domain calculations are in good agreement.

## 3.2. Comparative Analysis

As seen from Section 2.6, there are no error control parameters in the phase noise analysis. The accuracy of the PPVs, noise matrices and phase noise spectrum is completely determined by the properties and accuracy of the LPTV system obtained from the underlying PSS analysis. This is true with either the time-domain shooting method or the frequency-domain harmonic balance method. Furthermore, the phase noise simulation of a particular circuit also depends on the capabilities of the underlying PSS method to converge to the solution.

An extensive number of simulations were run to show how simulation parameters and problem size affect the phase noise calculation time and accuracy using both the frequency-domain and time-domain techniques implemented in our version of SPICE3. These simulations were run on a Sun Fire 280R workstation with 1.2GHz UltraSPARC III Cu processor and 8Gb of main memory.

### 3.2.1. Simulation Time and Scalability

The computation time for the frequency-domain phase noise analysis depends mostly on the size of the Jacobain matrix of the harmonic balance method at the PSS solution. The size of the Jacobian matrix depends on both the number of the circuit unknowns and the number of Fourier coefficients that represent the solution. In case of the time-domain approach, the phase noise computation time depends both on the size of the circuit matrix and the number of time points in one period of the steady-state solution.

A slight modification of the three-stage ring oscillator circuit from Section 3.1.1 was used for simulations. To increase the number of circuit unknowns, additional nodes were introduced in the circuit as in Figure 3.19. Each additional node (a, b, ...) adds a voltage ($v_a$, $v_b$, ...) to the list of unknowns.

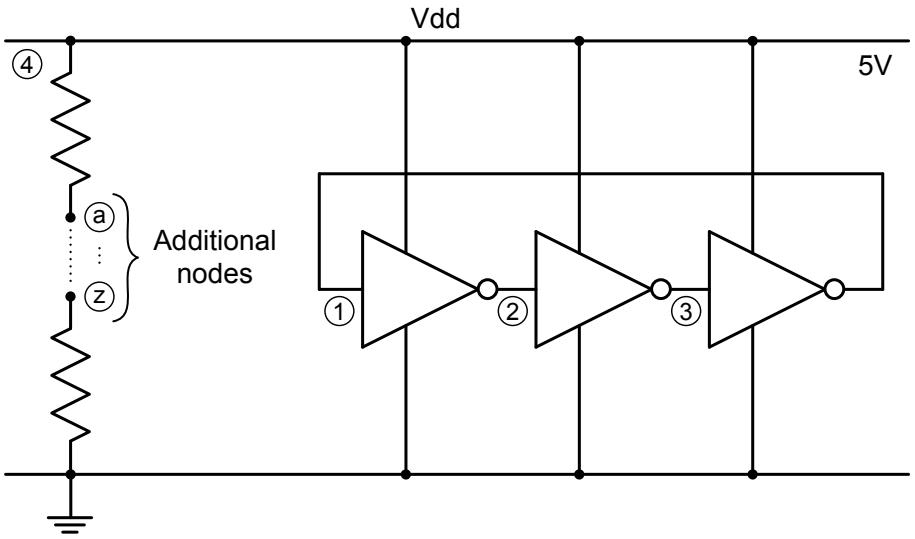


Figure 3.19. Schematic of a ring oscillator with additional nodes.

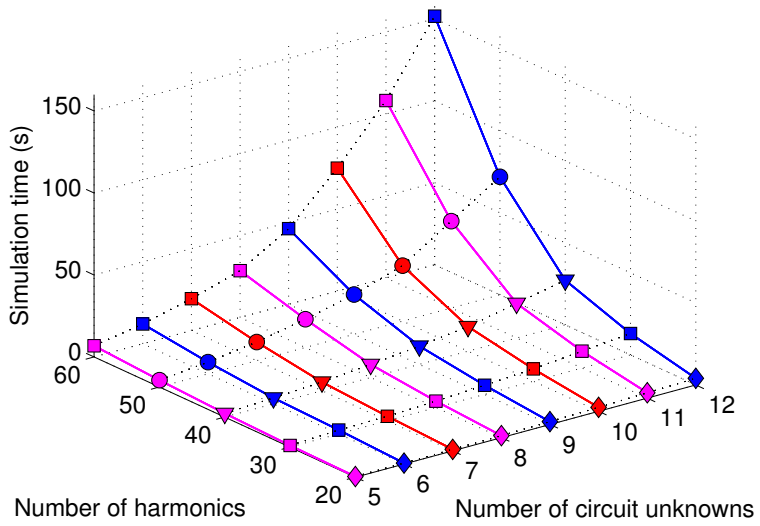


Figure 3.20. Harmonic balance based phase noise computation time surface.

Figure 3.20 shows the simulation time which forms a surface. This surface is a function of the coordinates of a two-dimensional space spanned by the number of circuit unknowns and the number of harmonics. The harmonic balance PSS simulation time is not included. The major contributor to the harmonic balance based phase noise computation time is the SVD calculation. Other operations, such as evaluations of noise sources, analytical differentiation in the frequency

domain, IFFT and computation of phase noise constants are insignificant, and their contribution is about 1% of the total time. The SVD computation time does not directly depend on the number of harmonics or on the number of circuit unknowns. It depends only on the matrix size, its sparsity and conditioning. Figure 3.21 shows the phase noise computation time as a function of the harmonic balance Jacobian matrix size. Theoretically, the algorithm chosen for singular

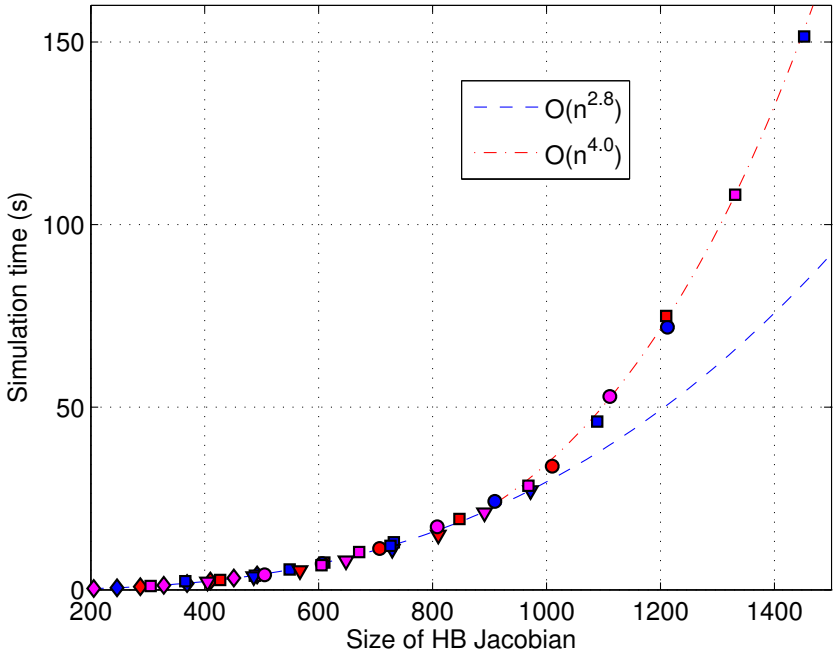


Figure 3.21. Harmonic balance based phase noise computation time.

value decomposition (see Section 2.6) computes the SVD of a dense matrix in $O(n^3)$ floating-point operations (flops) [15]. However, our time measurements show that the total simulation time scales as $O(n^{2.8})$ if the Jacobian size is less than 900×900 and as $O(n^{4.0})$ for larger matrices. This can be also seen form Figure 3.22 where both the simulation time and the size of the harmonic balance Jacobian are plot on a logarithmic scale. While working with large dense matrices, the simulation time does not only depend on the number of flops, but it also depends significantly on the computer memory organization. A larger amount

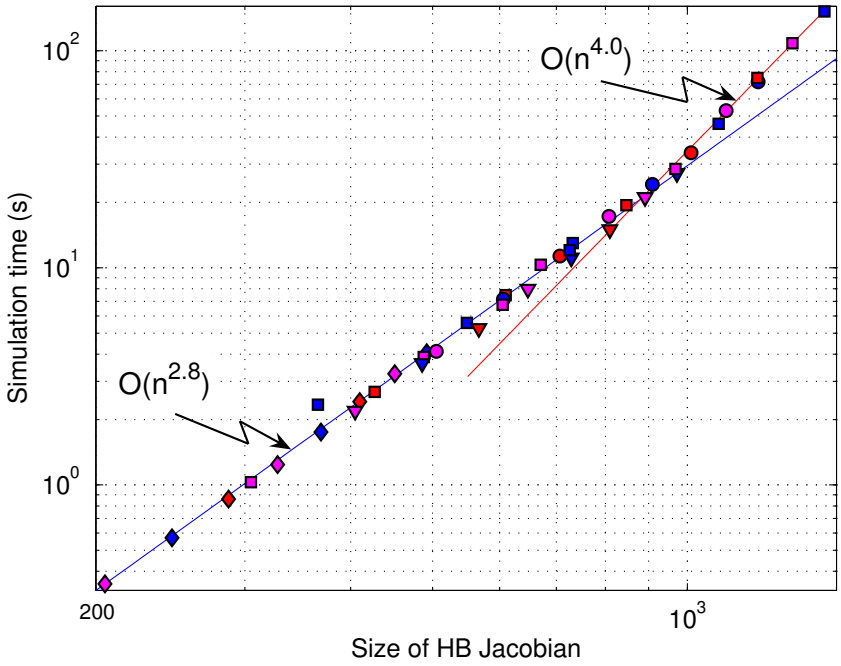


Figure 3.22. Phase noise computation time in logarithmic scale.

of cache helps to extend the range of problem scalability, as less operations with memory are needed. The Sun Fire 280R workstation has a 64Kb data cache on chip and an 8Mb external level-2 cache.

One way to improve the efficiency of the frequency-domain phase noise analysis is to use an SVD implementation optimized to work with large sparse matrices.

In our current implementation of the phase noise calculation based on a time-domain simulation [11], a single calculation of the monodromy matrix is the most time consuming part of the algorithm, as it involves operations with dense matrices. Figure 3.23 shows that the phase noise simulation time depends on the number of circuit unknowns and also on the number of time points per period of the PSS solution. The simulation time scales as $O(n^3)$ with an increase in the

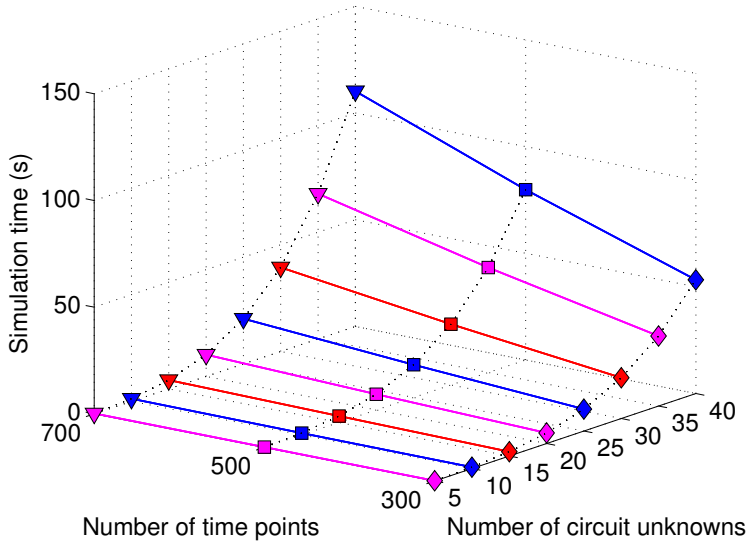


Figure 3.23. Time-domain based phase noise computation time surface.

number of time points, and it scales linearly with an increase in the number of circuit unknowns. The $O(n^3)$ scaling is due to dense matrix multiplications.

To gain an insight in the time for phase noise simulations of a large practical oscillator circuit, consider a differential three-stage ring oscillator shown in Figure 3.24. The oscillator consists of three Maneatis delay cells [22] shown in Figure 3.25.

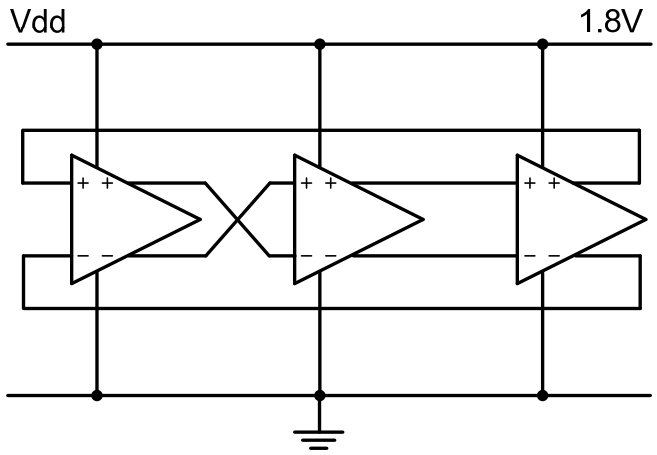


Figure 3.24. Block diagram of an oscillator with Maneatis delay cells.

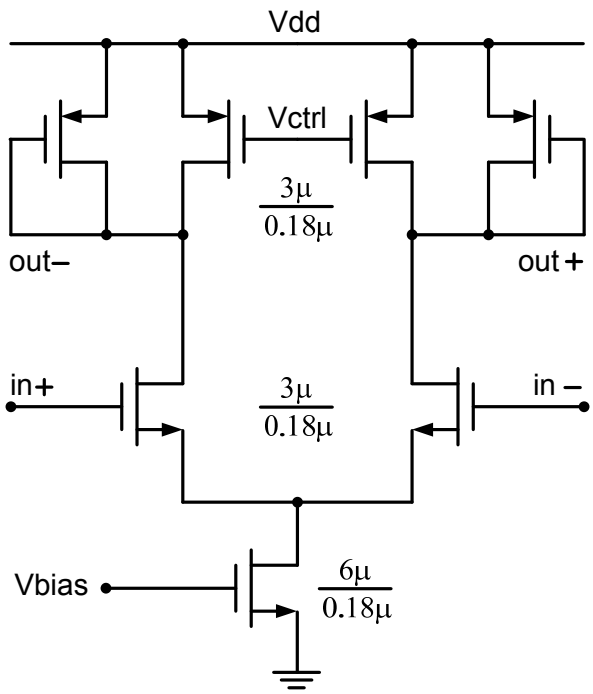


Figure 3.25. Schematic of the Maneatis delay cell.

| method | $N_{harm}$ | $N_{tpts}$ | *time* (s) |
|---|---|---|---|
| TD PSS | | 100 | 1.5 |
| FD HB | 15 | | 6.8 |
| TD PSS | | 500 | 7.7 |
| TD PSS | | 1000 | 15.0 |
| FD HB | 20 | | 15.9 |
| TD PSS | | 2000 | 30.1 |
| FD HB | 35 | | 125.9 |

Table 3.4. Phase noise calculation time for the Maneatis ring oscillator.

Table 3.4 shows the phase noise calculation time for a set of the time-domain and the frequency-domain simulations, where $N_{harm}$ is the number of harmonics, $N_{tpts}$ is the number of time points, and *time* is the phase noise com-

putation time. The rows of the table correspond to either the time-domain or the frequency domain simulations which are sorted in descending order of the phase noise computation speed. The tolerances for the Newton method convergence were fixed at $\varepsilon_{abs} = 10^{-12}$ and $\varepsilon_{rel} = 10^{-6}$.

Both the harmonic balance and shooting methods did not converge for $N_{harm}$ <15 and $N_{tpts}$ <100. All of the simulations resulted in less than 0.05dBc/Hz phase noise error. It is clear that for this circuit the time-domain shooting method is more efficient. The PSS simulation time is not included in Table 3.4, but in most cases the PSS of ring type oscillators is calculated more efficiently in the time domain than in the frequency domain [16]. This fact makes the time-domain simulation of the phase noise even more attractive.

One way to improve the performance of our time-domain implementation of phase noise analysis is to avoid the calculation of the monodromy matrix. If the time-domain phase noise analysis is based on Newton's shooting method that uses all circuit unknowns to compute the state transition matrix for the Jacobian calculation, then there is no need for an explicit monodromy matrix calculation. The monodromy matrix is the state transition matrix evaluated at time $T$. Unfortunately, in the current implementation of the shooting method [16] the time-domain Jacobian is not available in the desired form.

### 3.2.2. Accuracy

The accuracy of the PSS solution is crucial for an accurate phase noise calculation. The effect of time discretization in the time-domain shooting method and the effect of spectrum truncation in the harmonic balance method on the accuracy of phase noise calculation was studied. As in Section 2.6, a phase noise constant at 1kHz offset frequency was chosen to be a figure of merit for comparing the accuracy. To minimize other numerical factors that may affect accuracy

comparisons, the convergence criteria for all Newton loops used the same absolute and relative tolerances: $\varepsilon_{abs} = 10^{-12}$ and $\varepsilon_{rel} = 10^{-6}$. An exception is the outer Newton loop of the shooting method, which terminates when the following condition holds $|x(0) - x(T)| < 10^{-5}$.

Figure 3.26 shows the colored phase noise constant at 1kHz offset frequency

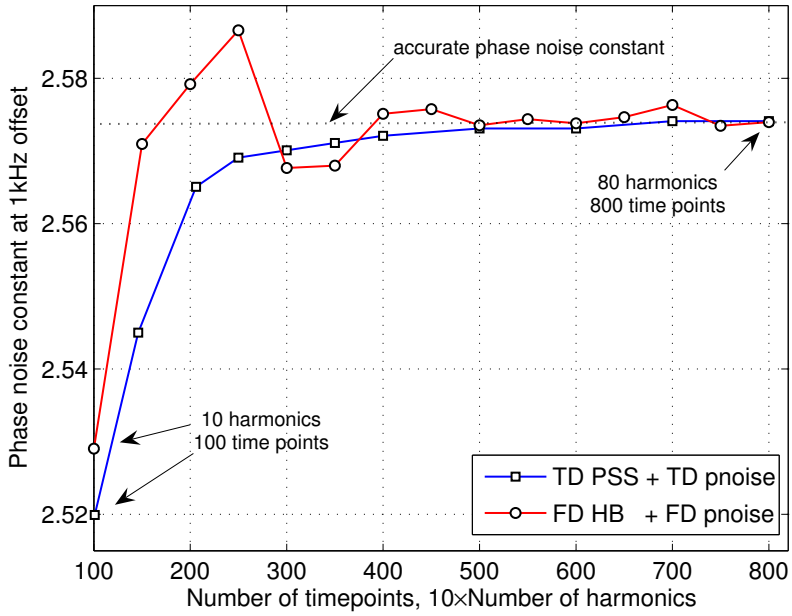


Figure 3.26. Phase noise constant as a function of PSS parameters.

as a function of the number of time points in case of the time-domain simulations and as a function of the number of frequencies in case of the frequency-domain simulations. In case of the time-domain simulations, the noise constant monotonically approaches its accurate value with a finer time discretization. In case of the frequency-domain simulations, the noise constant exhibits oscillatory settling to its accurate value. To understand this behavior, two more sets of calculations were conducted using 'hybrid' methods. The first method applies the frequency-domain phase noise calculation algorithm of Section 2.4.2 to the time-domain PSS solution obtained using the shooting method. The second method uses the frequency-domain harmonic balance to obtain the PSS and then the phase noise is

calculated using the time-domain algorithm of Section 2.4.1. The noise constant obtained using the four possible combinations, two original and two hybrid, are shown in Figure 3.27.

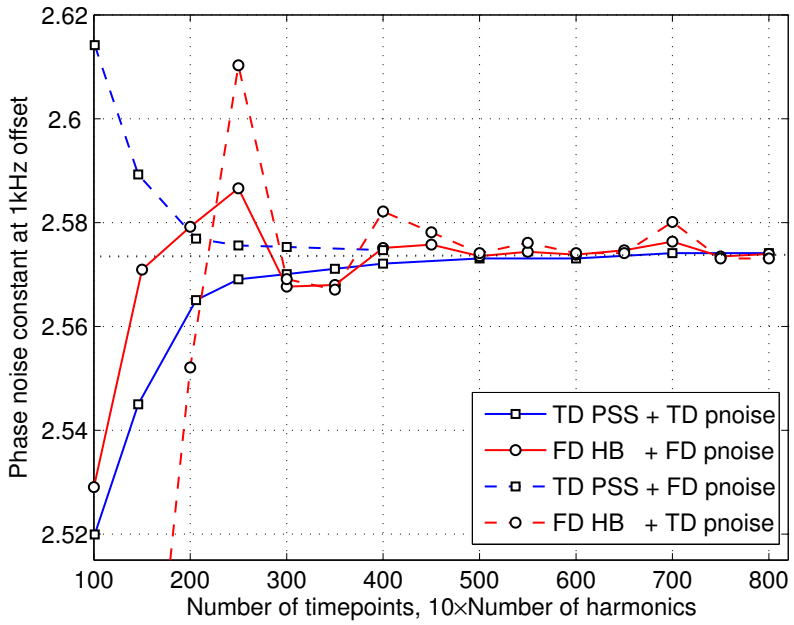


Figure 3.27. Phase noise constant obtained using original and hybrid methods.

From Figure 3.27 it is clear that the oscillatory convergence of the noise constant is a property of the PSS solution obtained from the frequency-domain harmonic balance method. A monotonic convergence of the noise constant is observed for the PSS solution obtained from the time-domain shooting method. Furthermore, given the same PSS solution, the noise constant is generally more accurate if it is calculated using the frequency-domain algorithm. This is because the derivative of the solution waveforms $\dot{x}_s(t)$ used to scale the PPVs (see Sections 2.4.1 and 2.4.2) is calculated analytically in the frequency domain, and it is more accurate than numerical differentiation in the time domain.

The oscillatory eigenvalue of the monodromy matrix and the minimal singular value of the Jacobian matrix can be used for estimating the accuracy of the PSS analysis, and therefore, for estimating the accuracy of the phase noise calcu-

lation. Table 3.5 shows the oscillatory eigenvalues $\lambda_{osc}$ and the minimal singular values $\sigma_{min}$ of two pairs of extreme cases from Figure 3.26, i.e., with 100 time points and 10 harmonics for the two inaccurate cases, and with 800 time points and 80 harmonics for the two accurate cases.

| PSS model | $\lambda_{osc}$ | $\sigma_{osc}$ |
|---|---|---|
| ideal | 1.0000 | 0.000000000 |
| accurate | 0.9998 | 0.000000365 |
| inaccurate | 0.9973 | 0.000103414 |

Table 3.5. Oscillatory eigenvalues and minimal singular values.

Figure 3.28 shows phase noise plots of the ring oscillator near the 1kHz offset frequency that correspond to accurate and inaccurate PSS simulations. The

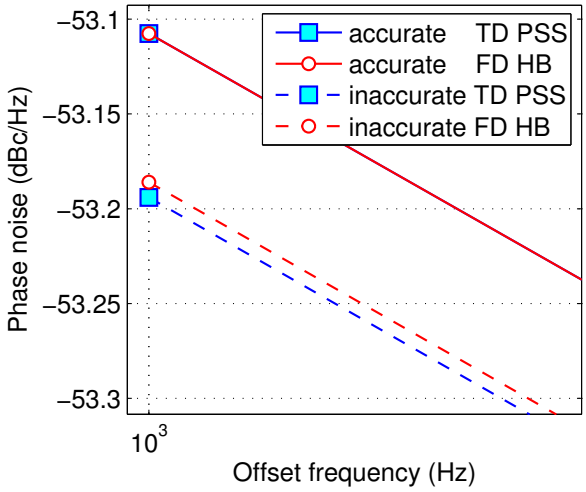


Figure 3.28. Phase noise with accurate and inaccurate PSS simulation.

phase noise simulation of the ring oscillator in the frequency domain using only 10 frequencies deviates from the accurate solution by less than 0.1dB. This is also true for a wide range of offset frequencies that are not shown in the figure.

The phase noise analysis is very insensitive to the time discretization and frequency truncation of the PSS solution of a well-conditioned problem, i.e., with a distinguishable oscillatory eigen mode. The ring oscillator example is a well-conditioned problem, as seen from Table 3.6. The oscillatory eigen mode of the

| **PSS model** | $\lambda_{oscillatory}$ | $\lambda_{decaying}$ | $\sigma_{null}$ | $\sigma_{range}$ |
|---|---|---|---|---|
| **accurate** | 0.9998151 | 0.0064416, ... | 0.000000365 | 0.002158781, ... |
| **inaccurate** | 0.9858087 | 0.0065689, ... | 0.000103414 | 0.002160419, ... |

Table 3.6. Distinguishable oscillatory eigen mode and null space.

ring oscillator can be easily distinguished from the eigen mode with the slowest decay rate even with an inaccurate time-domain PSS solution. The null space of the harmonic balance Jacobian can also be easily distinguished from its range space even with an inaccurate frequency-domain PSS solution. Some oscillators have eigen modes that are numerically indistinguishable from the oscillatory eigen mode [8]. In this case PSS analysis accuracy is of the highest priority during a phase noise analysis. A wrong selection of the eigen mode/null space will result in an incorrect phase noise calculation.

# 4. CONCLUSIONS

In this work, a frequency-domain harmonic balance based phase noise analysis was implemented in our in-house circuit simulator SPICE3. The phase noise analysis based on the time-domain response of an oscillator was modified to work in conjunction with the shooting method. Simulation results of a set of oscillator circuits were presented and described in detail. A comparative analysis of both the time-domain and the frequency-domain phase noise analyses in terms of accuracy, speed and scalability was conducted. Suggestions for improving the efficiency of these analyses were provided.

The current implementation of the time-domain phase noise calculation is more efficient than the frequency-domain implementation for comparable accuracies and practical problem sizes. The frequency-domain phase noise computation speed can be improved by using an SVD solver optimized to work with large sparse matrices. The time-domain phase noise analysis can be accelerated by computing the monodromy matrix from the shooting method Jacobian matrix at the PSS solution, instead of explicitly computing the monodromy matrix. The phase noise analyses can be easily modified to work with robust implementations of the PSS analysis, based on a homotopy transformation of the oscillator problem, available in our version of SPICE3 [23], [24].

In future work, a circuit simulator capable of phase noise and PPV simulation can be used for evaluating a cost function inside an automated phase noise performance optimization loop for voltage-controlled oscillators (VCO). The linearity and tuning range of a VCO can also be optimized. In this case a set of PSS and phase noise simulations has to be run to evaluate the cost function. Therefore, it is important to minimize the computation cost for phase noise calculations.

# BIBLIOGRAPHY

[1] A. Hajimiri and T. H. Lee, *The Design of Low Noise Oscillators*, Kluwer Academic Publishers, Boston, 2000.

[2] B. Razavi, "Challenges in portable RF transceiver design," *Circuits and Devices*, vol. 12, pp. 12-25, Sep. 1996.

[3] K. S. Kundert, J. K. White, and A. Sangiovanni-Vincetelli, *Steady-State Methods for Simulating Analog and Microwave Circuits*, Kluwer Academic Publishers, 1990.

[4] A. Demir, A. Mehrotra, and J. Roychowdhury, "Phase noise in oscillators: A unifying theory and numerical methods for characterization," *IEEE Trans. Circuits and Systems-I*, vol. 47, pp. 655-674, May 2000.

[5] F. Herzel and B. Razavi, "A study of oscillator jitter due to supply and substrate noise," *IEEE Trans. Circuits Syst. II*, vol. 46, pp. 56-62, Jan. 1999.

[6] U. Moon, K. Mayaram, and J. Stonick, "Spectral analysis of time-domain phase jitter measurements," *IEEE Trans. Circuits Syst. II*, vol. 49, pp. 321-327, May 2002.

[7] M. Farkas, *Periodic Motions*, Springer, Berlin, 1994.

[8] A. Demir, "Floquet theory and non-linear perturbation analysis for oscillators with differential-algebraic equations," *International Journal of Circuit Theory and Applications*, pp. 163-185, Mar-Apr. 2000.

[9] G. Floquet, "Sur les quations diffrentielles linaires  coefficients priodiques," Ann. cole Norm. Sup. 12, pp. 47-88, 1883.

[10] A. Demir "Oscillator noise analysis," *18th International Conference on Noise and Fluctuations*, Salamanca, Spain, Sep 2005.

[11] V. Kratyuk,"Algorithms and tools for optimization of integrated RF VCOs," *M.S. Thesis*, Oregon State University, Jun. 2003.

[12] J. W. Demmel, *Applied Numerical Algebra*, SIAM, Philadelphia, 1997.

[13] L. N. Trefethen and D. III Bau, *Numerical Linear Algebra*, SIAM, Philadelphia, 1997.

[14] http://www.netlib.org/lapack, *LAPACK home page*

[15] H. Ren, "On the error analysis and implementation of some eigenvalue decomposition and singular value decomposition algorithms", *Ph.D. Dissertation*, University of California, Berkeley, 1996, LAPACK working note 115, http://www.netlib.org/lapack/lawns/.

[16] Y. Hu,"Steady-state analysis techniques for coupled device and circuit simulation," *Ph.D. Dissertation*, Oregon State University, May 2004.

[17] X. Duan,"Frequency domain steady-state simulation of oscillators," *Ph.D. Dissertation*, Oregon State University, Jun. 2005.

[18] T. Quarles, A. R. Newton, D. O. Peterson and A. S. Vincentelli, *SPICE3f5 User's Manual*, University of California, Berkeley, Mar. 1994.

[19] BSIM3v3 Manual, University of California, Berkeley, 1996.

[20] C. Ho, A. E. Ruehli, and Brennan, "The modified nodal approach to network analysis," *IEEE Trans. Circuits and Systems*, vol. 25, pp. 504-509, Jun. 1975.

[21] V. Kratyuk, I. Vytyaz, U. Moon, and K. Mayaram, "Analysis of supply and ground noise sensitivity in ring and LC oscillators," *Proc. ISCAS 2005*, vol. 6, pp. 5986-5989, May 2005.

[22] J. Maneatis and M. Horowitz, "Precise delay generation using coupled oscillators," *IEEE J. Solid-State Circuits*, vol. 28, pp. 1273-1282, Dec. 1993.

[23] X. Duan and K. Mayaram, "Frequency domain simulation of high-Q oscillators with homotopy methods," *Proc. ICCAD 2004*, pp. 683-686, Nov. 2004.

[24] W. Ma, L. Trajkovic, and K. Mayaram "HomSSPICE: A homotopy-based circuit simulator for periodic steady-state analysis of oscillators," *Proc. ISCAS 2002*, pp. 645-648, May 2002.